Numerical Analyses and Optimizations on the Flow in the Nacelle Region of a Wind Turbine

Pascal Weihing[1], Tim Wegmann[1], Thorsten Lutz[1], Ewald Krämer[1], Timo Kühn[2], and Andree Altmikus[2]

[1]Institute of Aerodynamics and Gas Dynamics, University of Stuttgart, Pfaffenwaldring 21, 70563 Stuttgart, Germany
[2]Wobben Research & Development GmbH, Borsidgstraße 26, 26607 Aurich, Germany

Correspondence: Pascal Weihing (weihing@iag.uni-stuttgart.de)

Abstract. The present study investigates the flow dynamics in the hub region of a wind turbine focusing on the influence of the nacelle geometry on the root aerodynamics by means of Reynolds averaged Navier-Stokes simulations with the code FLOWer. The turbine considered is a generic version of the Enercon E44 converter incorporating blades with flatback-profiled root sections. First, a comparison is drawn between an isolated rotor assumption and a setup including the baseline geometry, in order to elaborate the basic flow features of the blade root. It was found that the nacelle reduces the trailed circulation of the root vortices and improves aerodynamic efficiency for the inner portion of the rotor, but on the other hand induces a complex vortex system in the junction of the blade and the nacelle that causes flow separation. The origin of these effects is analyzed in detail. In a second step, effects of basic geometric nacelle properties have been analyzed with the purpose to increase the aerodynamic efficiency in the root region. Therefore, three modification categories have been addressed, where the first alters the nacelle diameter, the second varies the blade position relative to the nacelle and the third comprises modifications in the vicinity of the blade-nacelle junction. The impact of the geometrical modifications on the local flow physics are discussed and assessed with respect to aerodynamic performance in the blade root region. It was found that increasing the nacelle diameter deteriorates the root aerodynamics, since the flow separation gets more pronounced. Possible solutions identified to reduce the flow separation are a shift of the blade in direction of the rotation or the installation of a fairing fillet in the junction between the blade and the nacelle.

1 Introduction

In recent years, upscaling of wind turbines has led to steadily increasing rotor diameters. Concepts beyond 10MW reveal diameters of more than 200m (Bak et al., 2017). With that development and the particular fact that aero-acoustic emissions and compressibility effects constrain the tip speed to around 80m/s, a possible measure to increase the overall rotor power is to increase aerodynamic forces in the inner blade sections. However, structural demands and geometric compatibility are dominant design factors over aerodynamic efficiency there, so that typically airfoils with high relative thickness are employed which are blended to cylindrical root sections. The poor aerodynamic performance of these sections involving massive flow separation and complex three dimensional flow structures are well known. It is easy to show that by assuming a linear increase of axial induction towards its optimum value along the radius for the inner third of the rotor, which is rather optimistic, it can

be shown that, C_P of the cannot exceed a value of $43/81$. This means a loss of 10.5% compared to the Betz value. In practice, the annual energy production loss in the root region can be estimated to around 3.5% (Loganathan and Gopinath, 2018). In order to increase rotor efficiency in its inner portion, a better understanding of the flow physics, in particular of the driving effects for flow separation, must be obtained.

1.1 Flow Separation on Conventional Blade Root Geometries and Rotational Effects

As previously mentioned, cylindrical root sections are common due to their structural benefits, cheaper manufacturing and easier transportation. Regarding their aerodynamic behavior, however, bluff body like separation is inevitable and even at the connecting thick "blending" airfoils strong trailing edge separation is often present in course of angle of attack and in particular thickness induced adverse pressure gradients in chord-wise direction. Once the flow detaches, the centrifugal force transports the fluid outwards in radial direction. During this motion, the fluid is subject to a Coriolis force accelerating the fluid again in chord-wise direction. These rotational forces are responsible for a delay of stall compared to an equivalent two dimensional section being commonly known as the Himmelskamp effect (Himmelskamp, 1947). Experimental studies on the rotational effects in the inboard sections have been conducted during NREL's Unsteady Aerodynamics Experiments by Schreck and Robinson (2002) who compared surface pressure data and forces on the rotating blades against analogous stationary conditions. During the MEXICO campaigns (Schepers and Snel, 2007), unsteady surface pressure as well as PIV measurements have been conducted which served as validation basis for studies on stall delay in the hub region by Herráez et al. (2014), Guntur and Sørensen (2015). At TU Delft, experimental investigations using PIV were performed with focus on the root flow of a two bladed model wind turbine (Akay, 2016). They could identify strong root vortices and high axial velocities in the root region. Recently, Herráez et al. (2016) performed numerical simulations on the same rotor and characterized the Himmelskamp effect as well as the origins of span-wise flow. A similar study has been conducted by Bangga et al. (2018) for the DTU 10MW rotor.

1.2 Corner Flow Separation of Aerodynamically Shaped Junctions

The wind turbine considered in the present study differs from conventional designs in the sense that it employs aerodynamically shaped profiles down to the nacelle. This has the benefit that by using suitable flatback airfoils flow separation could be generally eliminated when considering only the isolated blade without interference effects to other turbine components. It could be experimentally shown by Schreck et al. (2013) that for a full scale turbine employing flatback profiles flow separation was already negligible at $r/R = 0.14$. It must be pointed out that the turbine considered in that study employed a cylinder like connection to the hub, i.e. there was no distinct intersection length with the hub. In case that the airfoil shape is actually maintained towards the root, mutual interaction of the wall boundary layers occurs. The melded corner boundary layer is however less rich in kinetic energy and therefore prone to so called corner separation. This phenomena is typically found in the junction of the wing and the fuselage of transport aircraft (Levy et al., 2014; Vassberg et al., 2008) or in turbo-machinery cascades (Knezevici et al., 2010). Corner flows are highly influenced by a complex vortex system of primary and secondary vortices and have been investigated in great detail in the experimental work addressing the effect of the horseshoe vortex (HSV) near the leading edge (see review paper of Simpson (2001)) and more recent by Gand et al. (2015), focusing also on the trailing

edge and analyzing the corner vortex. The latter authors found particular evidence that the Reynolds stresses are not aligned with the mean shear tensor, which means that anisotropy of turbulence is present in the region of corner flow separation. Numerically, this makes corner flow separations very challenging to predict. From the NASA drag prediction workshops dedicated to aerodynamic predictions of a transport aircraft (Vassberg et al., 2008) a huge scatter in the separation bubble size of the wing-fuselage junction was obtained in the CFD predictions. Particularly the original version of the Spalart-Allmaras Turbulence model (Spalart and Allmaras, 1992) has shown to massively overestimate the bubble size. In order to reduce model uncertainty for these kinds of flows, NASA very recently initiated an own Junction Flow Experiment (Rumsey et al., 2016).

1.3 Scope and Objectives

The scope of the present study is to characterize the flow dynamics in the root region of a wind turbine with flatback airfoil segments and to elaborate the effects induced by the voluminous nacelle. Particular emphasis is placed on the driving parameters for root separation. In course of this, a modification of the nacelle geometry is introduced in three categories with the purpose to improve the aerodynamic behavior in the root region. First, the relative nacelle thickness shall be varied, followed by a variation of the blade position relative to the blade. Lastly, the effect of fillet-type geometry modifications in the blade-nacelle junction shall be discussed.

The next section gives an overview of all considered cases and modifications. In section 3 computational details on the flow solver, settings and grids are provided. The results addressing the above defined objectives are discussed in section 4 and the main conclusions are finally drawn in section 5.

2 Baseline Reference Turbine and Considered Modifications

Since the goal of the present study is to analyze the blade root aerodynamics of a flatback rotor and to identify the major geometric properties of the blade nacelle interaction, a generic reference turbine has been used. It is a generic version of the Enercon E44 turbine. The rotor diameter of this pitch regulated turbine is $44\mathrm{m}$. The induction distribution is similar to the original turbine, however, the original airfoils have been replaced by open source DU and NACA airfoils. Further, the flatback trailing edge segment is a purely generic design. The latter is responsible for a very high solidity of the rotor in the inner sections as shown in the upper left graph of Fig. 1. The baseline nacelle geometry, is drop-shaped with $L = 8.1\mathrm{m}$ length and a relative thickness of 48%. The point of maximum thickness is at $x/L = 0.39$. The cut position between the rotating hub and the static nacelle is at $x/L = 0.515$.

In order to isolate the governing fluid mechanical effects in the blade root region, different geometrical parameter sets will be addressed which are summarized in Fig. 1. The baseline case described above will be referred to as *CaseT1.0*. The general effects of the nacelle on the blade root flow shall be analyzed in comparison with an isolated rotor simulation (*CaseIsoRotor*). From that, it shall be assessed, whether the isolated rotor assumption holds for rotors with high solidity.

In a second step, the relative thickness of the nacelle is varied from the baseline, being increased by a factor of 1.2 and 1.4, obtaining the modifications *CaseT1.2* and *CaseT1.4*, respectively. For the latter case, the blade has been redesigned in the root

region involving a modified twist distribution (*CaseT1.4-twistMod*) which is shown in the upper left graph of Fig. 1. The twist angle has been increased in the root region by around $2°$ and approaches the original distribution at $r/R = 0.36$.

The next modification category addresses a variation of the blade position relative to the nacelle. These modifications are based on the nacelle with the largest thickness. *CaseT1.4-dXm04* denotes a blade shift in negative x-direction by 0.4m, whereas a movement of the blade in rotational direction by $\Delta y = \pm 0.5$m will be investigated in the cases *CaseT1.4-dYm05* and *CaseT1.4-dYp05*, respectively. Additionally, the movement of the blade in direction of rotation shall be applied to the baseline nacelle thickness, as well, yielding *CaseT1.0-dYm05*. The latter incorporates also a hump in the rear part of the suction side of the blade.

Lastly, the geometry in the junction will be modified. In *CaseT1.0-rounded*, the junction line has been rounded by a constant radius of $r = 0.4$m, whereas in *CaseT1.0-fairing*, the radius has been blended from $r = 0.2$m at leading edge and on the pressure side to $r = 0.85$m at the trailing edge of the suction side.

3 Computational Details

3.1 Flow Solver and Numerical Settings

For the present study, the block-structured finite volume solver of the compressible Navier-Stokes equations FLOWer (Kroll et al., 2000) by DLR has been used. This code is well suited for simulation of rotary wings, since the fluxes caused by relative grid movements are taken into account. Thereby, the movements of the different components are realized with the overset grid technique (Benek et al., 1986). At the authors' institute, FLOWer is continuously developed to improve simulation capabilities of rotary wings, including high order schemes (Kowarsch et al., 2013), advanced turbulence modeling (Weihing et al., 2016), fluid structure interaction Sayed et al. (2016), wake modeling Weihing et al. (2017), and optimization for high performance computing (Letzgus et al., 2018).

In the present study, the discretization of the Euler fluxes is based on central differences with artificial dissipation according to Jameson et al. (1981) using a $k4$ value of 128. Unless otherwise stated all simulations are performed steady state. For unsteady simulations, a dual time stepping discretization according to Jameson (1991) is used. Viscous fluxes are discretized by central differences. Regarding turbulence equations, FLOWer uses a fully implicit discretization and has implemented several one- and two-equation models, as well as Reynolds stress closures. Unless otherwise stated all simulations are conducted fully turbulent using the k-ω-SST model by Menter (1994). As discussed in Appendix A this model is able to predict primary vortices in junction flows and showed good agreement with experiments regarding the extent of corner flow separation.

3.2 Grids and Boundary Conditions

The set-up for the simulations considers a periodic $120°$ segment of the flow problem and comprises the meshes for the rotor blade and the nacelle which are embedded into a background grid. For topological reasons, the connection of blade and nacelle
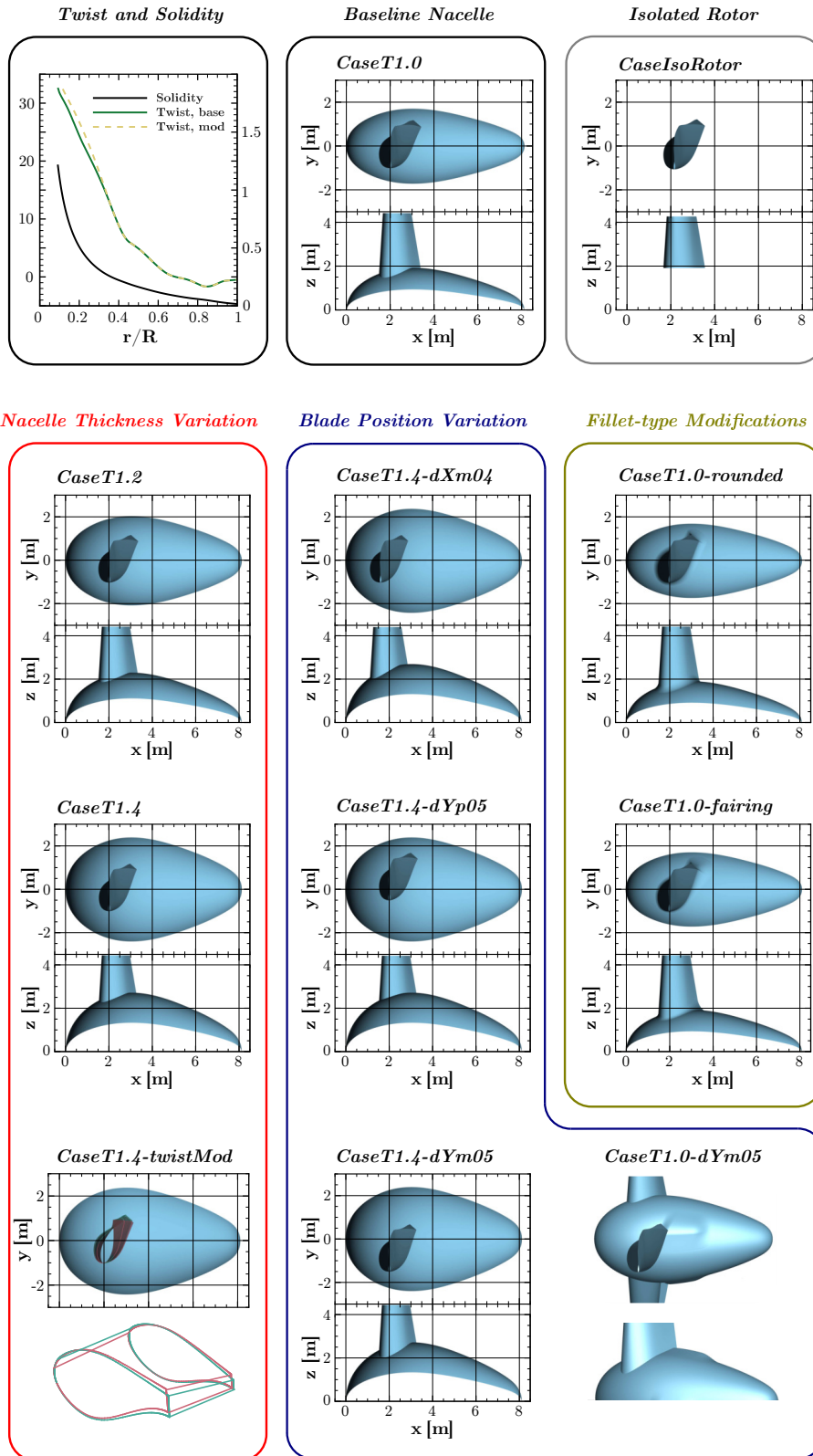
Figure 1. Considered geometric variations of the blade-nacelle region.

in *CaseT1.0-rounded* and *CaseT1.0-fairing* uses an independent grid, being created manually. All other grids were generated automated by using appropriate *Gridgen* and *Pointwise* scripts, in order to obtain consistent results for all cases.

The polar background mesh extends 24 rotor radii upstream and downstream and 13 radii in radial direction. It contains $448 \times 192 \times 128$ cells in stream-wise, radial and circumferential direction. The grid spacing near the blade is $0.15\text{m} \times 0.3\text{m}$ in the rotor plane.

The mesh of the nacelle covers the whole blade grid and serves as refinement for the root region of the blade. The boundary layer spacing is adapted on the Reynolds number assuring $y_p^+ \approx 1$. The geometric stretching factor is 1.1 and comprises 64 extrusion layers. The edge cell size of the latter is equally extended in radial direction up to $r/R = 0.25$ to adequately refine the root region. In circumferential and stream-wise direction 320 and 168 cells are used, respectively.

The rotor blade is meshed in a two stage process. All cases use the same blade mesh for $r/R > 0.17$. This part was generated using the *Automesh* script for rotor blade meshing developed at IAG. It is of C-H topology with a H-block extension of the tip using 288×168 cells in circumferential and radial direction, 64 cells on the trailing edge and 60 cells in the wake. Again, a Reynolds number adapted first cell height was chosen and the near wall region is resolved with 64 layers implying a growth rate of 1.11. In the second stage the blade mesh is extended in a conformal way to the individual nacelle, including again 64 cells to refine the boundary layer region of the corner. A detailed view of the surface meshes of the blade-nacelle intersection is depicted in Fig. 2 showing the refinement in the junction as well as the overlapping of the grids.

CaseT1.0 and *CaseT1.4* have been also simulated using the inviscid Euler equations. For those simulations, the grids have been modified by removing all boundary layer refinements which was necessary to achieve converged solutions.

As mentioned before, the rounding of the junction in the cases *CaseT1.0-rounded* and *CaseT1.0-fairing* does not allow for the previously described grid topology. A high quality grid with smooth cell distributions and as little as possible skewness could only be obtained by manually meshing the blade connector. This was conducted in O-type topology and is shown in Fig. 3.

The integration of the blade mesh into the nacelle mesh is illustrated in Fig. 4. In total, a typical set-up consists of around 50Mio grid points.

Regarding the boundary conditions, the $120°$ domains are mapped periodically and the global domain boundaries carry far-field conditions. All surfaces are treated as no-slip walls (except for the additional Euler simulations of *CaseT1.0* and *CaseT1.4*). However, for the nacelle only the upstream part, the spinner, is rotating (Fig. 4 yellow colored patches), whereas the rear part (brown colored patches) stays fixed. This is achieved in the rotating grid setup without chimera or sliding mesh interfaces under exploitation of periodicity by subtracting the boundary velocity from the value of the interior cell, before setting the ghost layers.

3.3 Simulation Parameters and Operating Conditions

All simulations are conducted at a wind speed of $U_\infty = 10\text{m/s}$ which is the optimal point of maximum power coefficient. The tip speed ratio is $\lambda = 6$ and pitch, tilt and cone angles are zero. The simulations have been performed steady state for $150,000$ iterations. To verify convergence, the simulations have been continued unsteadily by five more revolutions using a time step
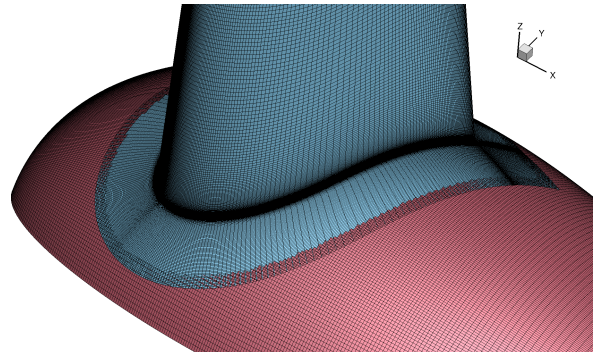
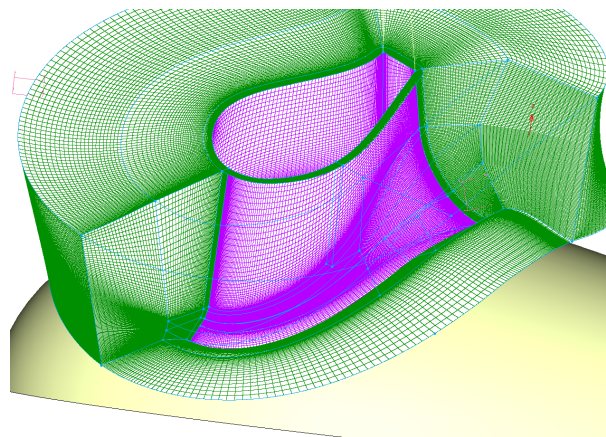**Figure 2.** Surface grid in the vicinity of the blade root-nacelle junction.

Figure 3. Grid topology for the fairing modification.

equivalent to $0.25°$ azimuthal movement. The averaged thrust coefficient of the fifth revolution deviates by less than 0.01% from the averaged value of the last $10,000$ iterations of the steady-state solution. Besides of the integral values, the fluctuations of the radial force distribution in the root region were very small, since only shallow flow separation prevails. For these reason and the fact that computational time can be significantly reduced, all results presented in the following are based on steady-state

5   solutions. However, it is clear that for detailed analyses addressing the unsteady behavior of the separated region, unsteady or even scale resolving simulation techniques must be applied.

4   Results

In this main section of the paper the simulation results of the different parameter groups shall be discussed, starting with a comparison of the rotor including the nacelle with the isolated rotor and subsequently analyzing specific geometric variations,

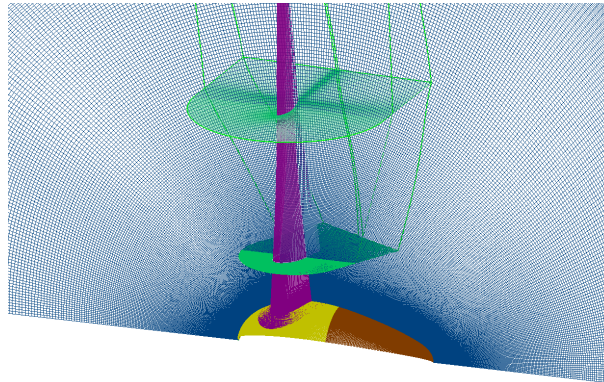10   as relative nacelle thickness, blade position and junction shape.

Figure 4. Integration of the blade mesh into the nacelle grid.

4.1 General Effects of the Voluminous Nacelle

To investigate the general effects of the nacelle on the blade root aerodynamics, the cases *CaseIsoRotor* and *CaseT1.0* are compared. The flow field will be characterized showing relevant coherent structures, three-dimensional effects and stall are going to be addressed. A digression will be made on the challenges of determining the AoA in the root region, before the effect
5   of the nacelle on the aerodynamic coefficients will be summarized.

4.1.1 Vortical Structures

A first impression of the flow field can be gained by visualizing the dominant vortical structures using the Λ_2 criterion as well as the axial velocity distribution in the center cut, as shown in Fig. 5. For *CaseIsoRotor* the typical root vortices emerge from balancing the bound circulation at the root. The contour color of the iso-surface denotes the vorticity in y-direction and indicates
10   the expected sense of rotation. The normalized axial velocity u/U_∞ in the slice shows a distinct jet through the hub which is responsible for the relatively high advance rates of the root vortices. Apart from those, no other relevant vortical structures are present that might indicate e.g. flow separation. Turning to *CaseT1.0*, shallow flow separation is visible on the suction side near the junction with the nacelle. Moreover, the dominant root vortex seen before has vanished. As will be discussed in more detail in Sec. 4.2, the vortices spiraling around the nacelle evolve from the two vortex legs of the HSV generated in the blade-nacelle
15   junction. As the convecting velocity is significantly smaller than in *CaseIsoRotor*, these vortices which are counter-rotating come very close to each other until eventually, mutual interaction occurs. This results into the formation of three dimensional turbulent structures in the wake of the nacelle. The application of eddy resolving simulation techniques such as DES could bring further insight into these interaction phenomena (Weihing et al., 2016).

An effect that could be identified to enhance the generation of turbulent structures in the nacelle wake is the consideration
20   of both, the rotating spinner and the steady rear part of the nacelle. In previous simulations during the project, where the entire nacelle had been rotated, these structures were almost absent (Kühn et al.). In order to elaborate the effects of the boundary layer roll up and detachment in the rear part of the nacelle, isolated simulations of only the spinner and the static rear part of
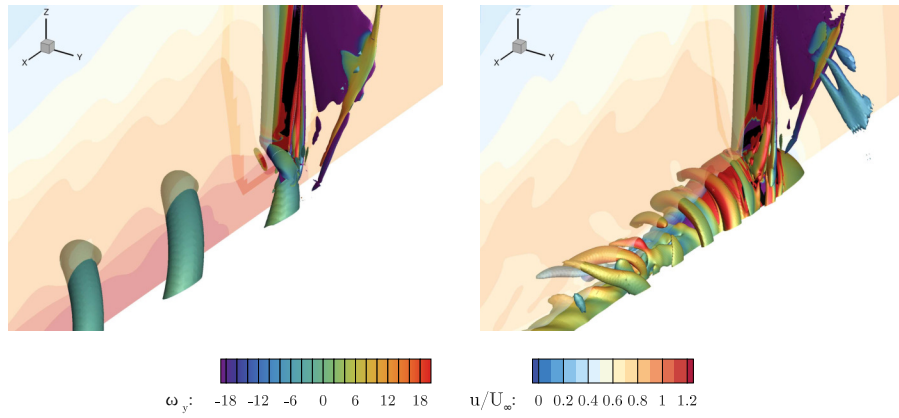
Figure 5. Vortices in the root area visualized by a Λ_2 iso-surface for *CaseIsoRotor* (left) and *CaseT1.0* (right). The vortices are colored by vorticity in y-direction. The $x = 0$ slice shows the normalized axial velocity component.
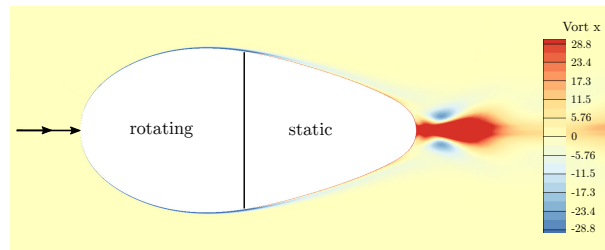

Figure 6. Vorticity in stream-wise direction in the boundary layer of an isolated nacelle including only the spinner and the static rear part.

the nacelle have been conducted. The vorticity in stream-wise direction evaluated in the inertial frame of reference is shown in Fig. 6. The spinner is rotating in positive convention around the x-axis and accelerates the surrounding fluid that has no circumferential component far off the wall and therefore generates a negative x-vorticity above the spinner. At the interface to the non-rotating nacelle part, this accelerated layer is suddenly retarded again inducing a positive x-vorticity in the near

5   wall region above the static part of the nacelle. It results into a growing shear layer with positive circumferential velocity that detaches from the nacelle in the rear part forming spiraling longitudinal vortices.

An additional effect seen in both cases indicated by the wavy velocity distribution at around $r/R = 0.3$ is dedicated to trailing vortices associated with span-wise gradients of bound circulation. However, its strength appears to be significantly lower compared to the vorticity directly at the root.

10   **4.1.2   Three Dimensional Flow and Separation in the Root Region**

The extent of the flow separation as well as three dimensional flow patterns can be retrieved from the surface streamlines on the suction side of the blade shown in Fig. 7. For *CaseIsoRotor* there is no flow separation at the root. The slight radial flow component is dictated by the root vortex rolling from the pressure to the suction side. This is also reflected in the velocity

contours in a slice $x = 2$m just cutting the leading edge of the blade. The plotted velocity contours indicate the deviation velocity $\tilde{w}$ describing the vertical motion relative to the ideal circular path. Negative values as for *CaseIsoRotor* therefore mean that the streamlines stem from further outboard than assumed from kinematics.

By including the nacelle, its displacement effect evokes an effective inclination angle in that plane which results in a positive deviation component $\tilde{w}$. For the inner 20% of the rotor it is more than 0.5m/s. The negative values at around $r/R = 0.3$ are subject to the induction of the mid-trailing vortex described in the previous section. At the inboard sections, a clear flow separation evolves from the junction with the nacelle. It spreads in radial direction and realigns with chord direction at about $r/R = 0.17$. When focusing on the pressure contours, those are mostly parallel for *CaseIsoRotor* except for the very inboard region that is directly influenced by the root vortex. For *CaseT1.0* significant curvature of the isobars is visible in the area covered by the dividing streamline. As part of the separation process it can be observed that the angle of the shear stress vector turns relative to the pressure gradient, indicating a complex interaction of centrifugal-, Coriolis- and pressure forces as drivers of the three dimensional flow. Due to the very high solidity (c/r) of the blade, which varies between 1.1 at $r/R = 0.1$ and 0.5 at $r/R = 0.2$ a high impact of three dimensional effects can be expected.

To estimate the share of these forces acting in the yz-plane, the simple balance can be written for a rotation around the x-axis as

$$0 = - \begin{pmatrix} \frac{\partial p}{\partial y} \\ \frac{\partial p}{\partial z} \end{pmatrix} + \rho \begin{pmatrix} \Omega^2 y \\ \Omega^2 z \end{pmatrix} + \rho \begin{pmatrix} 2\Omega w \\ -2\Omega v \end{pmatrix}, \tag{1}$$

where the second and third term denote the centrifugal and Coriolis forces, respectively. The velocity components v and w are acting in chord- and span-wise direction relative to the moving blade rotating with Ω. As can be directly seen in the equation, by definition, the Coriolis force vanishes when the velocity is tangential to the rotation, hence it is expected to be small directly above the nacelle. For the balance in span-wise direction the Coriolis force changes sign with respect to the chord-wise velocity component, acting inward for attached flow and outward for separated flow and particularly vanishing near the dividing streamline. In contrast to that, the centrifugal force component in span-wise direction is simply proportional to the z-coordinate. Therefore, at the point of separation, the only force to hold the fluid particle on the path of rotation would be a span-wise pressure gradient dp/dz. The latter can be derived from the radial pressure distribution plotted in Fig. 8 for different chord-wise sections. At $x_c/c \approx 0.5$ which is close to the separation point, there is virtually no span-wise pressure gradient. Hence, the fluid moves outward solely due to the centrifugal force. It would accelerate towards the tip due to the increasing centrifugal force with z, if there was no Coriolis force. As the outward movement is naturally connected with a positive w-component it deflects the flow in chord-wise direction and once there is a chord-wise component and a positive v-velocity an additional inward deflection is induced, until finally, the flow aligns again with the chord direction. The transport of separated fluid in outward direction is known as centrifugal pumping (Lindenburg, 2003) and allows for a pressure recovery also in radial direction, where the adverse pressure gradient is smaller compared to the chord-wise section (see e.g. $x_c/c \approx 0.85$). For equivalent two-dimensional conditions, most of the pressure recovery would therefore occur in the turbulent mixing of the airfoil wake. This explains the commonly observed stall delay of a rotating blade compared to equivalent two-dimensional conditions (e.g. (Lindenburg, 2003), (Snel et al., 1993)).
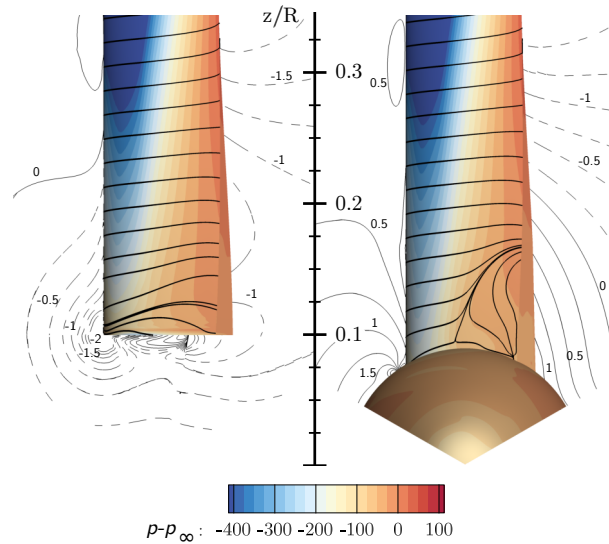
Figure 7. Visualization of three dimensional flow in the root region using streamlines and pressure contours on the suction side of the blade for *CaseIsoRotor* (left) and *CaseT1.0* (right). The contour lines indicate the "deviation velocity" $\tilde{w}$ from to the ideal kinematic value $-\Omega y$ in a slice at $x = 2$m.

The current investigations supports the studies of Du and Selig (2000), Lindenburg (2003) and recently Herráez et al. (2016) who explained the radial flow with the centrifugal force as well. In this study, the significantly higher blade solidity using the flatback airfoils down to the nacelle indicates significant impact of three dimensional effects.

Turning to the front part of the blade, it can be shown that following Bernoulli's principle, the static pressure decreases in radial direction due to the increasing dynamic pressure of the inflow. This results in an outward pressure gradient. However, it is not believed to be the only reason for the slight radial component of the streamlines near the leading edge, since first, the pressure gradient is balanced by the Coriolis force in z-direction and further, a strong acceleration in chord-wise direction prevails, which is in accordance with Schreck and Robinson (2002). As described in more detail in Sec. 4.3 it is seen to be connected with an effective sweep angle of the blade relative to the inflow direction. This is again an effect of the high solidity of the blade which results into a leading edge shift relative the rotational axis in y-direction. Comparing the pressure levels, the suction peak is significantly reduced in *CaseIsoRotor* due the induction of the root vortex over the whole inner portion of the rotor.

4.1.3   Determination of the Angle of Attack in the Root Region

In order to assess the aerodynamic performance of the individual blade sections in terms of aerodynamic coefficients and to utilize that information in two-dimensional approaches such as BEM or for airfoil design tools, it is essential to accurately determine the angle of attack (AoA) from the three-dimensional flow field. However, it is clear that its extraction is far from trivial as wind velocity and rotation are superimposed by the induction of the wake and the bound circulation of the blade
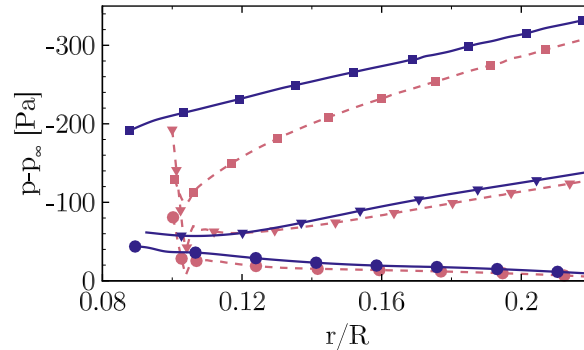
Figure 8. The effect of the nacelle thickness on the radial pressure distribution on the suction side, at $x_c/c \approx 0.1$ (squares), $x_c/c \approx 0.5$ (triangles) and $x_c/c \approx 0.85$ (circles) for *CaseIsoRotor* (dashed), *CaseT1.0* (solid)

itself. Most approaches such as those compared by Rahimi et al. (2017) aim to eliminate the effect of the bound circulation. They provide very similar results at the mid-board blade sections. However, at the blade tip and root, major differences were observed. For the root region those were explained by the massive flow separation in the wake of the very thick airfoils. As for the present rotor flow separation is only shallow, or even absent, differences between the AoA extraction methods are strongly

5   linked to the effects of the root vortex system, instead of the dominant vortex shedding caused by massive flow separation. Therefore, two AoA evaluation methods shall be compared with focus on the root region.

The first is the *Reduced Axial Velocity* method (RAV) of Johansen and Sørensen (2004), which eliminates the bound circulation by azimuthally averaging the axial velocity for each radial section. Secondly, the *Line Average* method of Jost et al. (2018) is applied which averages the velocity vector along closed lines around the blade. Both methods are sketched in Fig. 9.

10   As seen in the figure, for the *Line Average* method, the extraction of the velocities occurs along circles that are curved about the rotational axis with a radius corresponding to the location of the quarter-chord point in each section, being centered around the latter. The radius of the projected circle is one chord length. By averaging the planar velocity vector along these curves, Jost et al. (2018) could show that the effect of bound circulation can be eliminated resulting in the pure inflow conditions for that section. The evaluation of the AoA in Fig. 10 shows a lower AoA near the tip for the *Line Average* method, since it locally

15   accounts for the induction of the tip vortex, which is smeared out by the azimuthal averaging in the RAV method (c.f. Fig. 9). Accounting for the local induction is a desired feature of the *Line Average* method and has shown to accurately reconstruct the inflow conditions for corresponding two-dimensional analyses of the near tip region (Jost et al. (2018) and Rahimi et al. (2017)). Near the blade root, the AoA predicted by the *Line Average* method is higher than obtained by the RAV method. The reason for this is that the azimuthal arc length for averaging the axial velocity in the RAV method is now smaller compared to

20   averaging over the circular line of the *Line Average* method (c.f. Fig. 9). Particularly, the acceleration of the curving stream-lines upstream of the airfoil are not considered in the RAV method. This effect becomes particularly important for *CaseT1.0*, where both the blade and the nacelle displace the flow and therefore accelerate it upstream of the leading edge which is the reason why the increase of AoA is more pronounced for the case including the nacelle. Additionally, it must be noted that for
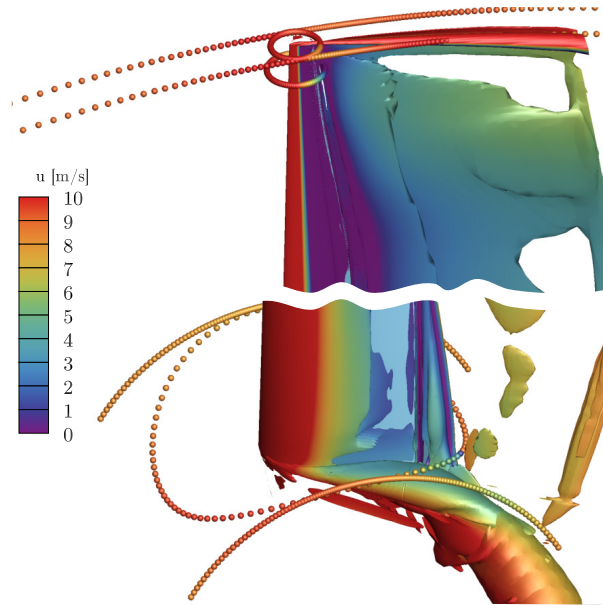
Figure 9. Extraction of axial velocity in the inertial frame near the tip and the root using the *Reduced Axial Velocity* method (Johansen and Sørensen, 2004) (circular arcs) and the *Line Average* (closed curves) (Jost et al., 2018) method.
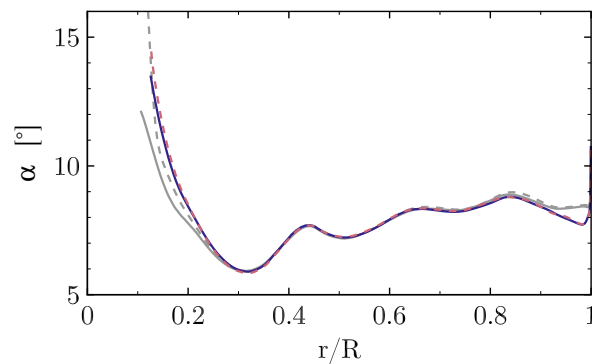

Figure 10. Radial distribution of the angle of attack for *CaseIsoRotor* (dashed) and *CaseT1.0* (solid) using the RAV method (gray) and the *Line Average* method (colored).

the RAV method the root vortex is occupying about 40% of the downstream arc length, being more concentrated for the *Line Average* method. As a consequence the latter predicts a higher axial velocity in the rotor plane compared to the RAV method (c.f. Fig. 11), and therefore a higher AoA. In the remainder of the paper, the AoA will be evaluated with the *Line Average* method.
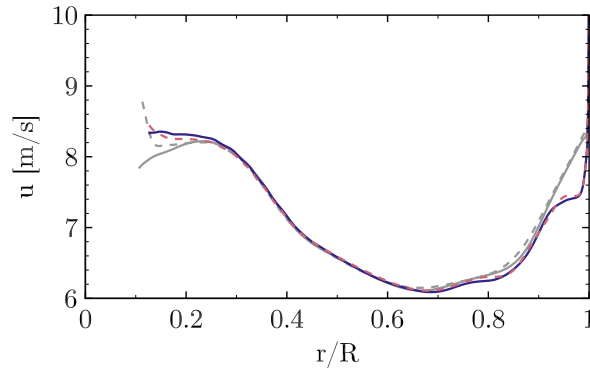
Figure 11. Radial distribution of the axial inflow velocity for *CaseIsoRotor* (dashed) and *CaseT1.0* (solid) using the RAV method (gray) and the *Line Average* method (colored).

4.1.4 The Effect of the Nacelle on Aerodynamic Coefficients

The pressure coefficient C_p is compared for the configurations *CaseIsoRotor* and *CaseT1.0* as well as two-dimensional airfoil simulations in a slice at $r/R = 0.136$ (Fig. 12). Following Bernoulli's principle, the pressure coefficient has been normalized using the maximum dynamic pressure that can be exploited from the kinematics $q_{\infty,rot} = \rho/2 \left(U_\infty^2 + (\Omega r)^2 \right)$. In accordance

5   with the independence principle of swept wing theory, only the component normal to the leading edge is relevant for the aerodynamic properties. Therefore, the z-coordinate has been used as radius for the circumferential component in the dynamic pressure. It should be noted that one could also account for the induction and sweep angle effects, but then the reference state gets rather ambiguous and is difficult to compare among the different cases. Hence, it will be accepted that with the kinematic normalization, C_p might differ from 1 in the stagnation point and it will be attempted to explain this with the dominant physical

10 effects.

As already discussed in the previous section, the induction of the root vortex significantly diminishes the suction peak for *CaseIsoRotor*. For the rotor including the nacelle, the pressure level is lower for the entire suction side of the blade, particularly in the front part of the airfoil. Hence higher lift and lower pressure drag can be expected for *CaseT1.0*. At the pressure side the differences are small. Only directly at the stagnation point a higher pressure coefficient is obtained by *CaseIsoRotor*, which is

15 slightly > 1. This can be explained by the negative $\tilde{w}$ contours (Fig. 7) which indicate that the fluid hitting the airfoil is actually stemming from further outboard compared to its ideal kinematic path. Therefore, fluid of higher momentum is transported towards the leading edge part of the airfoil, yielding a higher stagnation pressure than assumed for normalization. By contrast, in *CaseT1.0* the stagnation pressure is lower than estimated, due to an effective inclination angle which pushes fluid from the inboard sections to the reference cut. Finally, focusing on the aft chord region, it can be confirmed that also for *CaseT1.0* the

20 cut is outside of recirculation and that pressure is almost recovered by the centrifugal pumping mechanism.

To further assess the three-dimensionality of the flow in the hub region, a comparison shall be drawn with two-dimensional simulations. Those were performed at the angles of attack $\alpha = 10.2°$, $13°$ and $14°$, where the first corresponds to the extracted
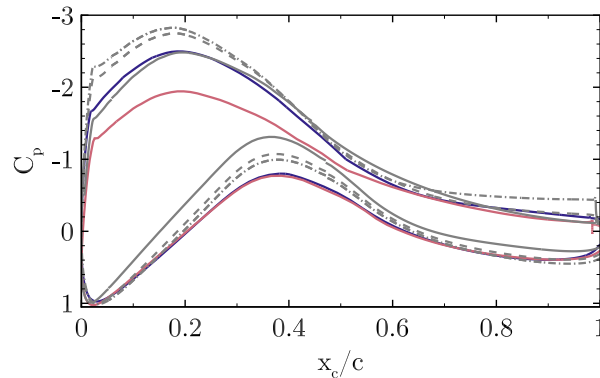
Figure 12. Pressure coefficient C_p at $r/R = 0.136$ for *CaseIsoRotor* (solid red) and *CaseT1.0* (solid blue) compared with two-dimensional simulations (gray lines): $\alpha = 10.2°$ (solid), $\alpha = 13°$ (dashed), $\alpha = 14°$ (dashed dot).

value from the RAV method for *CaseT1.0*, the second corresponds to a slightly higher value obtained from the *Line Average* method which was $12.3°$ for *CaseT1.0* and the last is close to the AoA obtained for increased nacelle thicknesses as shown in Sec. 4.2. The 2D results at $\alpha = 10.2°$ reveals no separation. At $\alpha = 13°$ shallow trailing edge separation is present which moves forward to $x_c/c \approx 0.6$ at $\alpha = 14°$. Compared to the 3D results, *CaseIsoRotor* shows a completely different behavior

5   which cannot be mimicked by any 2D simulation. At a first glance the level of the suction peak of *CaseT1.0*, suggests that $\alpha = 10.2°$ would be a good approximation. However, it must be pointed out that when scaling the stagnation pressure in the 3D results to a value of 1, the distribution increases a bit. Moreover, the visual inspection of corresponding streamline plots compared in that section (not shown here) clearly suggested a larger AoA than $10°$. The distribution in the adverse pressure regime is very similar to the 2D results at $\alpha = 13°$ implying a similar boundary layer stress. The differences on the pressure

10 side are also markedly, showing distinctly stronger suction peaks predicted by any of the two-dimensional simulations. These examinations emphasize the strong three-dimensionality of the flow in the root region of the present rotor and point out that the application of two dimensional polars in BEM without correction models must be treated with caution, even if there is no massive flow separation.

The radial distribution of the circulation Γ plotted in Fig. 13 a), as well as the lift coefficient (Fig. 13 b)) confirm the

15 improvement of the aerodynamics in the root region by including the nacelle which effectively diminishes the harmful inductive effect of the root vortex. This is also reflected in a reduction of the drag coefficient (Fig. 13 c)) by up to 100 drag counts, although *CaseT1.0* involves flow separation. The region of influence of the nacelle extends to $r/R = 0.35$. By integrating the driving force within that range, this results in a higher torque of around 20% for that portion and one blade.

4.2   The Impact of the Relative Nacelle Thickness

20 From the previous section it was concluded that an improvement of the aerodynamic properties in the inner portion of the rotor could be obtained by including the nacelle. The attenuation of the root vortex by the nacelle diminished induced drag and
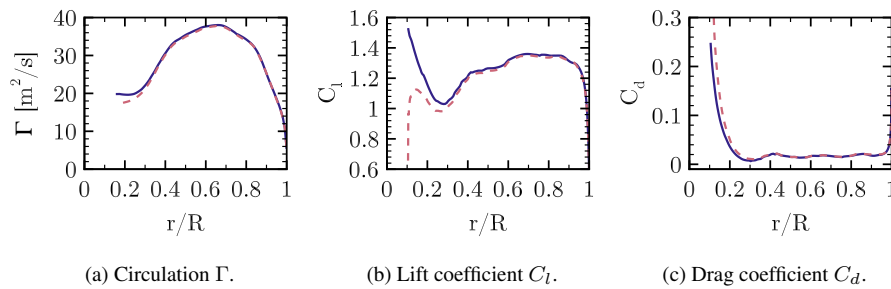
(a) Circulation Γ.   (b) Lift coefficient C_l.   (c) Drag coefficient C_d.

Figure 13. Distribution of aerodynamic coefficients along the blade radius for *CaseIsoRotor* (dashed) and *CaseT1.0* (solid).
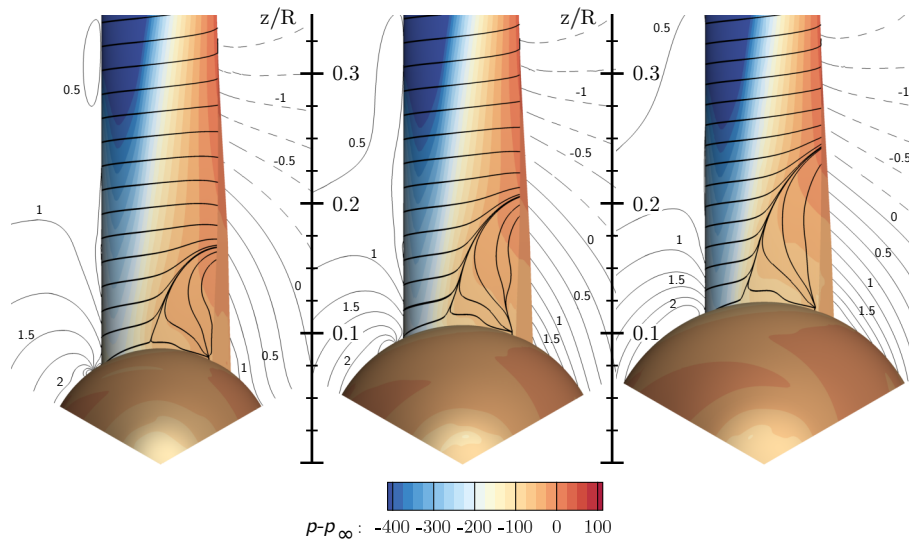

Figure 14. Visualization of three dimensional flow in the root region using streamlines and pressure contours for *CaseT1.0* (left), *CaseT1.2* (mid) and *CaseT1.4* (right). The contour lines are plotted for a slice at $x = 2$m and indicate the velocity $\tilde{w} = w - \Omega y$ which denotes the deviation from the ideal kinematic path.

increased lift. In this section the effects of the relative nacelle thickness shall be analyzed. The thickness has been increased in two steps by a factor of 1.2 and 1.4 (*CaseT1.2*, *CaseT1.4*), respectively.

4.2.1 The Effect on Flow Separation and its Driving Parameters

The resulting surface streamlines and pressure contours shown in Fig. 14 indicate growing flow separation with increasing nacelle thickness. The extent of the separation measured from the maximum nacelle thickness to the radial position of reattachment increases from $0.08R$ over $0.10R$ to $0.12R$ with nacelle thickness. From *CaseT1.0* to *CaseT1.4* the separation line moves forward by around 15%. In addition, it can be noted from the "deviation velocity" $\tilde{w}$ that the inclination of the inflow increases with larger relative nacelle thickness.
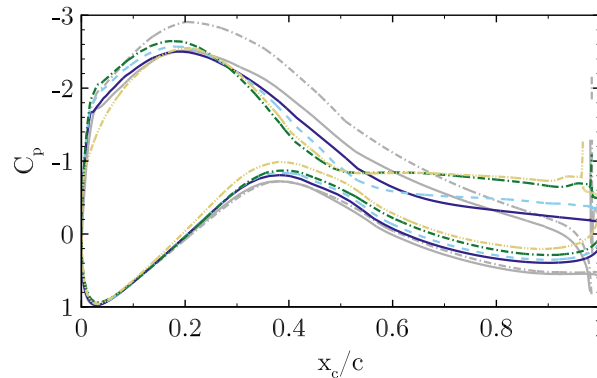
Figure 15. Airfoil pressure distribution at $r/R = 0.136$ for *CaseT1.0* (solid), *CaseT1.2* (dashed), *CaseT1.4* (dashed dot) and *CaseT1.4-twistmod* (dashed dot dot). The gray curves denote corresponding inviscid simulations.

The comparison of the pressure coefficient in the reference cut at $r/R = 0.136$ (Fig. 15) confirms the increasing separation for larger nacelle thicknesses. The distinct pressure plateau already suggests a loss of aerodynamic efficiency due to flow separation. The radial pressure gradients in the front part of the blade (Fig. 19) show that greater relative nacelle thickness increases the suction force due to the displacement effect of the nacelle. Also, in the mid- and aft- chord region the initial

5   pressure level is lower, which increases the radial adverse pressure gradient. Since separation inherently alters the pressure distribution, it is difficult to distinguish between the causes and affects of the flow separation. In order to assess whether stronger adverse pressure gradients develop by increasing the nacelle thickness, inviscid reference simulations have been performed for *CaseT1.0* and *CaseT1.4*. The interaction of the inviscid pressure fields is visualized in Fig. 17 using vectors of static pressure acting on the surfaces. For *CaseT1.0* the flow accelerates moderately in the junction, reaching the minimum of pressure at about

10   $x_c/c \approx 0.5$-0.6. It can be shown that the adverse pressure gradient imposed by the nacelle is slightly shifted behind the one from the blade. Turning to *CaseT1.4* this is not the case anymore, as the suction peaks fairly coincide at around $x_c/c \approx 0.3$-0.4. Downstream of that point the adverse pressure gradient markedly increases compared to *CaseT1.0* and is accordingly devolved on the blade as shown in Fig. 15. In *CaseT1.0* the inviscid and viscous suction peaks closely coincide, whereas a significantly higher peak prevails for the inviscid simulation of *CaseT1.4*, which clearly suggests that the boundary layer of the associated

15   viscous case is being increasingly loaded with larger nacelle thickness. From these investigations it can be concluded that a reduction of separation might be achieved by decoupling the interfering pressure gradients of the nacelle and the blade as it is typically conducted for winglets.

A second aspect, that turned out to be crucial for the development of the flow separation is directly linked to the vortex system evolving in the junction of the blade and the nacelle. The motivation for a detailed look into that came across, by analyzing

20   AoA behavior with respect to the different nacelle geometries (Fig. 20), where an increasing AoA of around two degrees could be observed from *CaseT1.0* to *CaseT1.4*. Hence, it was assumed that the increasing separation was also an effect of the larger AoA. Therefore, it was attempted to re-design the blade in order to compensate the AoA leading to *CaseT1.4-twistMod* which
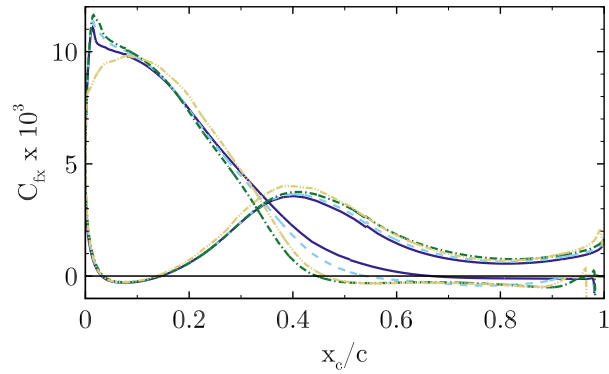
Figure 16. Airfoil skin friction distribution at $r/R = 0.136$ for for *CaseT1.0* (solid), *CaseT1.2* (dashed), *CaseT1.4* (dashed dot) and *CaseT1.4-twistmod* (dashed dot dot).
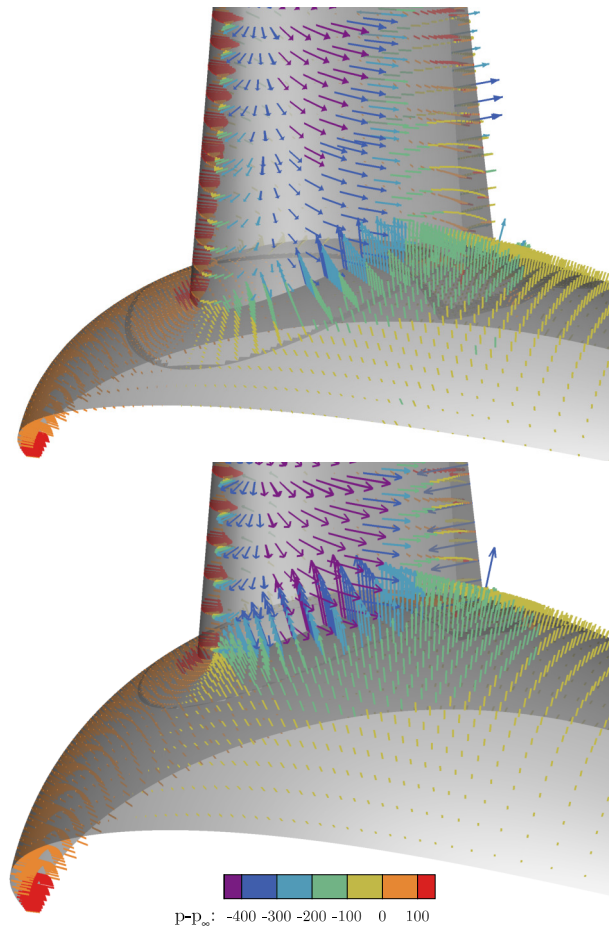

Figure 17. Inviscid pressure distribution in the junction region of blade and nacelle for *CaseT1.0* (upper) and *CaseT1.4* (lower).

employs an increased twist angle in the blade root region of around $2.0°$ (see Fig. 1). Except for the sections very closely to the root, where the aerodynamic behavior is obviously strongly non-linear and the *Line Average* method showed increasing axial velocities as consequence of an axial re-direction of the flow caused by the twist modification, the AoA could be effectively reduced. When coming back to the pressure distribution in Fig. 15, the suction peak is nevertheless reduced. The evaluation of
5 chord-wise skin friction (Fig. 16) shows that the separation remains almost the same as for *CaseT1.4*, so it could be concluded that flow separation is not directly affected by an AoA induced adverse pressure gradient on the blade.

It is more seen to depend on the interacting boundary layers in the junction region of the blade and the nacelle. For this purpose, the emerging vortices in the junction are visualized in Fig. 18 for *CaseT1.0* and *CaseT1.4* using volume stream-lines colored by their vorticity. Additionally, volume cuts are placed normal to the blade at the leading edge and at $x_c/c =$
10 $[0.25; 0.5; 0.75]$, respectively. The horseshoe vortex (HSV) is clearly visible being generated in the stagnation region as the boundary layer of the nacelle approaches the blade. It is rolling inward and its size and strength could be observed to increase with larger nacelle thickness. This behavior is consistent with Simpson (2001), who reports a stronger HSV with increasing AoA. Gand et al. (2015) experimentally showed that the onset of corner separation is delayed by a stronger HSV, since fluid of higher momentum is pushed into the blade boundary layer. This beneficial inductive effect, however, depends on the distance
15 to the blade. By increasing AoA the suction side leg departs from the blade and is further deflected by the Coriolis force for the present cases.

Directly inboard of the HSV, at the stagnation point the counter rotating corner vortex (CV) evolves which closely follows the junction line of the blade and the nacelle. Its production depends on the velocity gradients of the interacting boundary layers and its strength was observed to increase for the larger relative nacelle thickness in the adverse pressure gradient region.
20 In contrast to the HSV, the CV remains aligned with the junction. Due to its sense of rotation it is seen to deform the near wall velocity profile on the blade and to pull the boundary layer flow away from the wall. For all cases it was observed that the recirculation area was initiated from the streamline originating in the CV. Thus, high vorticity in the CV might be a main driver for the whole separation process. In particular it should be noted that the configuration with modified blade twist (*CaseT1.4-twistMod*) revealed quasi identical values for the CV strength as *CaseT1.4* and showed the same amount of
25 separation.

The second strategy for diminishing the detrimental flow separation could therefore be a mitigation of the blade-nacelle boundary layer interaction, in order to influence the CV strength and propagation. This aspect shall be investigated in Sec. 4.4.

4.2.2 The Effect of the Relative Nacelle Thickness on Aerodynamic Coefficients

To summarize the effects of the relative nacelle thickness on the aerodynamic coefficients in the root region which are plotted
30 in Fig. 20, those confirm the degradation of aerodynamic performance due to the enhanced separated flow in the inboard region, where lift mostly decreases and particularly drag increases. The AoA increases with nacelle thickness since reduced lift decreases axial induction yielding higher axial velocities in the rotor plane. The decrease of aerodynamic efficiency is most prominent for the inner 25% of the rotor radius. It should be noted that there was no measurable benefit for the outer
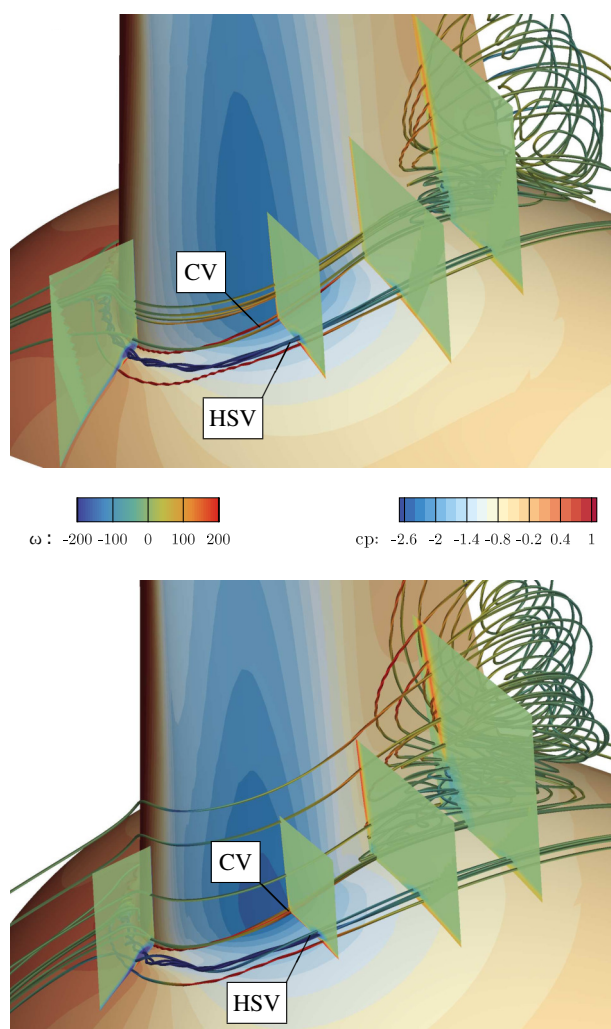
Figure 18. Vortex system in the junction of blade and nacelle for *CaseT1.0* (upper) and *CaseT1.4* (lower).
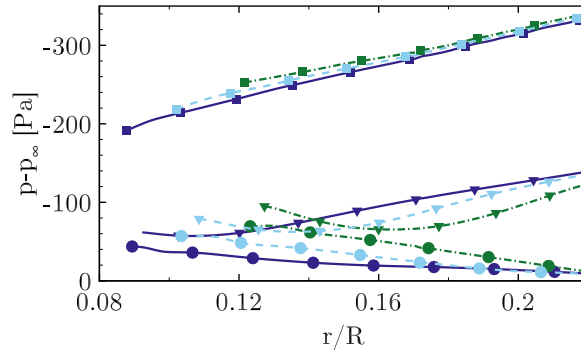
Figure 19. The effect of the nacelle thickness on the radial pressure distribution on the suction side, at $x_c/c \approx 0.1$ (squares), $x_c/c \approx 0.5$ (triangles) and $x_c/c \approx 0.85$ (circles) for *CaseIsoRotor* (dashed), *CaseT1.0* (solid), *CaseT1.4* (dashed dot).
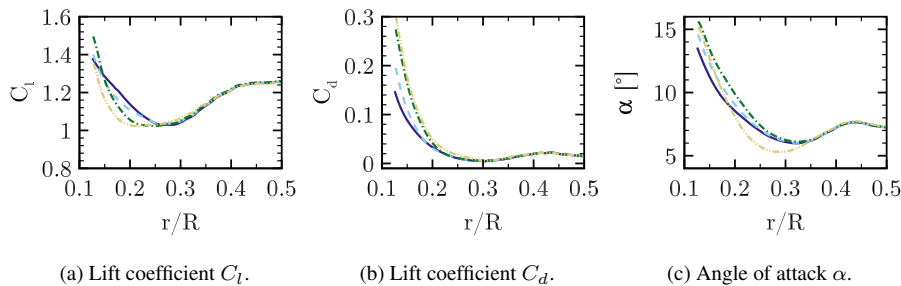

(a) Lift coefficient C_l.   (b) Lift coefficient C_d.   (c) Angle of attack α.

Figure 20. Aerodynamic coefficients along the blade radius for *CaseT1.0* (solid), *CaseT1.2* (dashed), *CaseT1.4* (dashed dot) and *CaseT1.4-twistmod* (dashed dot dot).

rotor sections as one might have expected due to a displacement effect of the nacelle. In total, rotor torque decreased for *CaseT1.CpThickness4* by 3.54% compared to *CaseT1.0*.

4.3 Movement of the Blade Position Relative to the Nacelle

As pointed out in section 4.2.1, a segregation of the interacting pressure gradients of the blade and the nacelle could reduce the
5 overall loading on the corner boundary layer. In order to analyze these effects, the blade was shifted upstream in axial direction
(*CaseT1.4-dXm04*), as well as upstream- and downstream in circumferential direction (*CaseT1.4-dYm05* and *CaseT1.4-dYp05*,
respectively). All modifications were based on the nacelle with the largest of the considered thicknesses, since first, the strongest
effects on the flow separation might be present there, and further, this configuration provides more space for relative blade shifts.
The motivation for the first modification was to place the entire blade in front of the point of maximum nacelle thickness and,
10 therefore, locate it in the favorable pressure gradient in axial direction. The shifting of the blade in y-direction correspondingly
aims to investigate the relative location of the pressure gradients in circumferential direction. Bangga (2018) investigated the
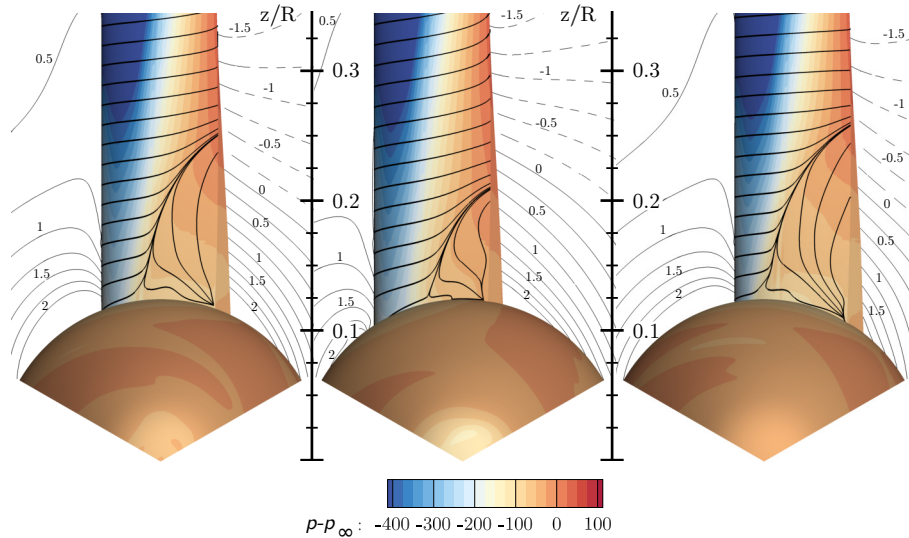
Figure 21. Visualization of three dimensional flow in the root region using streamlines and pressure contours for *CaseT1.4-dXm04* (left), *CaseT1.4-dYm05* (mid) and *CaseT1.4-dYp05* (right). The contour lines are plotted for a slice at $x = 2$m ($x = 1.5$m for *CaseT1.4-dXm04*) and indicate the velocity $\tilde{w} = w - \Omega y$ which denotes the deviation from the ideal kinematic path.

lateral shift of rotating profiles for the first time and focused on the exploitation of the y-component of the centrifugal force in Eq. 1 to increase rotor performance.

4.3.1 The Effect of the Relative Blade Position on Flow Separation

Comparing the surface streamlines plotted in Fig. 21 with those of the centered version (Fig. 14) moving the blade forward
5 in axial direction shows to have no improvement regarding the extension of the corner separation. Indeed, even a slight deterioration is present, which might be caused by the fact that the inclination angle relative to the blade increases. Turning to *CaseT1.4-dYp05*, an increase of the separation extent by around 8% can be observed compared to *CaseT1.4*, with separation beginning close behind 30% chord. A significant improvement can be achieved by shifting the blade in direction of rotation. The separation size in radial direction is $0.086R$, being only slightly above the baseline *CaseT1.0* but already smaller than in
10 *CaseT1.2*.

    The boundary layer profiles (Fig.22) shall be adduced to assess the mass flow rate of recirculation in the reference cut $r/R = 0.136$. At $x_c/c = 0.5$, *CaseT1.4-dYm05* is still attached, whereas slight and moderate back flow is observed in *CaseT1.4* and *CaseT1.4-dYp05*, respectively. Turning to the profiles at $x_c/c = 0.75$, the height of separation massively increases when shifting the blade in positive y-direction. As seen in Fig. 21 this seems to be linked with the volume covered by the downward curvature
15 after the point of maximum nacelle thickness in circumferential direction and might be "felt" by the blade boundary layer as an additional expansion, which goes along with added adverse pressure loading. This effect is weaker for *CaseT1.4-dYm05*, where most of the pressure recovery is achieved forward to that point.
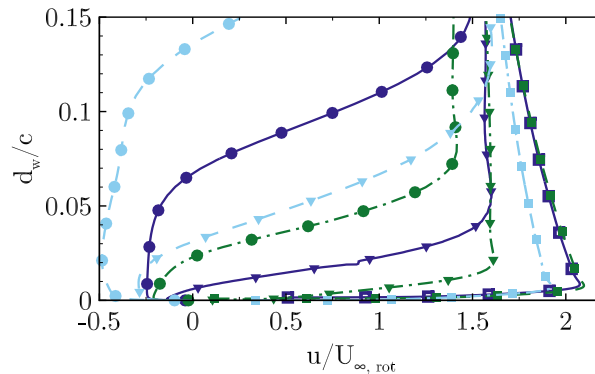
Figure 22. Stream-wise normalized velocity in the boundary layer $u/U_{\infty,rot}$ at $r/R = 0.136$ and $x_c/c = [0.25; 0.5; 0.75]$ (squares; triangles; circles), for *CaseT1.4* (solid), *CaseT1.4-dYm05* (dashed dot) and *CaseT1.4-dYp05* (dashed).
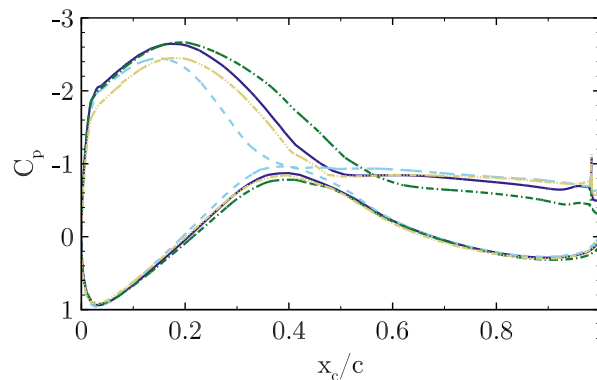

Figure 23. Airfoil pressure distribution at $r/R = 0.136$ for for *CaseT1.4* (solid) *CaseT1.4-dXm04* (dashed dot dot), *CaseT1.4-dYm05* (dashed dot) and *CaseT1.4-dYp05* (dashed).

In a similar way, the chord-wise (Fig. 23) pressure distributions are affected in accordance to previous observations. In *CaseT1.4-dXm04*, the suction peak decreases, but the kink to the pressure plateau remains at the same position as for *CaseT1.4*. In the aft-chord region, pressure recovery has still not initiated as it might be "blocked" by the displacement effect of the ascending nacelle diameter in the vicinity of the blade suction side. In *CaseT1.4-dYp05*, the massive flow separation yields a
5   collapse of lift at $x_c/c \approx 0.4$, which results in a reduced suction peak. Both cause a tremendous increase of pressure drag. The latter can certainly be reduced for *CaseT1.4-dYm05*, where moderate separation begins at $x_c/c \approx 0.65$. The downward slope shows that the last part of the pressure recovery already occurs along the airfoil and not predominantly in the wake, as for the other cases.

Regarding the span-wise pressure distribution (Fig. 24), a slight increase of suction force can be noted near the leading edge
10   in *CaseT1.4-dYm05* for the whole inner portion, whereas it is markedly lower when moving the blade in the other direction. In contrast to the other cases, *CaseT1.4-dYm05* maintains the slope of the leading edge cut, also along $x_c/c = 0.5$. Particularly,
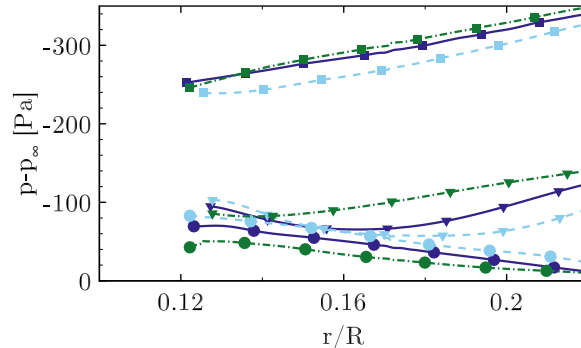
Figure 24. The effect of the blade position on the radial pressure distribution on the suction side, at $x_c/c \approx 0.1$ (squares), $x_c/c \approx 0.5$ (triangles) and $x_c/c \approx 0.85$ (circles) for *CaseT1.4* (solid), *CaseT1.4-dYp05* (dashed), *CaseT1.4-dYm05* (dashed dot).

CaseT1.4-dYp05 already shows the behavior typically found near the trailing edge, where pressure recovery is redeployed in radial direction by the centrifugal pumping mechanism. Consistently at $x_c/c = 0.85$, the radial pressure gradient is smallest in *CaseT1.4-dYm05*, since less recirculating mass needs to be transported outward, which directly yields an earlier realignment of the streamlines in chord-wise direction as seen in Fig. 21.

5   From the previous investigations in Sec. 4.2.1 using the Euler simulations, it became clear, that a decoupling of the adverse pressure gradients seems necessary to relief the boundary layer in the junction. As could be shown the axial shifting did not yield any improvement, so that it can be deduced that the predominant pressure gradient is the one in lateral direction. This seems also reasonable as the flow in the junction is aligned with that direction. As the adverse pressure gradient imposed by the nacelle initiates at the outmost point in circumferential direction, it follows that the entire pressure recovery

10 is additionally loaded in *CaseT1.4-dY05*. Opposed to that, the segregation of the adverse pressure gradients seems to work for *CaseT1.4-dYm05*.

    Another important aspect to be considered is already attributed to the inflow. As shown by the left sketch in Fig. 25, the inner sections of the forward shifted blade are affected by inflow stemming from an effectively larger radius with greater momentum. Along the airfoil the flow is pushed downward compared to its ideal kinematic path, which means that it is

15 effectively streaming from larger to smaller radius. According to conservation of angular momentum this results in acceleration, being supportive to overcome the pressure gradient. When crossing the xz-plane a corresponding retardation would prevail, which additionally reduces angular velocity in *CaseT1.4-dYp05*. To illustrate this inflow hypothesis, a velocity difference plot between *CaseT1.4-dYm05* and *CaseT1.4* shall be analyzed for the reference cut $r/R = 0.136$ in Fig. 25. For this, the solution of *CaseT1.4-dYm05* was back-shifted on top of the centered version. For the entire front part of the airfoil a higher velocity

20 magnitude prevails, which is particularly present inside the boundary layer as seen before in Fig. 22. In the stagnation region the inflow velocity is $\approx 1\mathrm{m/s}$ higher for *CaseT1.4-dYm05* compared to *CaseT1.4*. Another distinct peak, where the velocity is markedly higher for *CaseT1.4-dYm05* is found in the region of adverse pressure at around $x_c/c \approx 0.5$. In the rear part of the airfoil the differences originate from the different thickness of the separated wake.
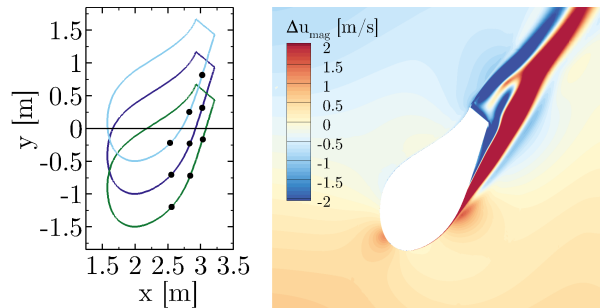
Figure 25. Sketch of the shifted profiles at $r/R = 0.136$ (left). Difference in velocity magnitude between *CaseT1.4-dYm05* and *CaseT1.4* (right).

The third effect that is seen to be beneficial for delay of separation by shifting the blade in direction of rotation is the sweep angle of the inflow vector with respect to the blade leading edge. At the reference cut it is more than $25°$ for *CaseT1.4-dYm05*, about $17°$ for *CaseT1.4* and around $9°$ for *CaseT1.4-dYp05*. In radial direction the sweep angle decreases exponentially, but is still greater than five degrees at the tip for *CaseT1.4-dYm05*. As the flow turns about the airfoil, the effective sweep angle is not

5   constant along the chord-wise direction, but since most of the lift is generated in the front portion of the blade, it can certainly be stated that sweep effects cannot be neglected. This is supported by the streamlines in *CaseT1.4-dYm05* (Fig. 21) that show the typical pattern found for swept wings at high AoA (Obert, 2009), featuring a distinct attachment line instead of a stagnation point, which results in $C_{p,max} < 1$, as well as a prominent span-wise deflection of the streamlines near the trailing edge. In contrast to that, the streamlines remain approximately perpendicular to the leading edge in *CaseT1.4-dYp05*. The question,

10 whether the principle of independence holds or not is certainly debatable, since rotation introduces span-wise gradients to the flow field. Indeed, for attached boundary layers it is a typical assumption made in BEM codes and is also supported by analyses of Leishman (1989). At high AoA in the stall regime it is generally not valid anymore. However, as observed in the boundary layer profiles (Fig. 22), the streamlines (Fig. 21) and pressure distribution (Fig. 23), there is evidence that the sweep angle delays stall and is beneficial for reattachment as it stimulates the outward centrifugal pumping mechanism. An overview of

15 the effect of sweep angle on dynamic stall can be found in the text book of Leishman (2006). Measurements reinforcing the present observations regarding the effect of sweep angle on maximum lift coefficient and stall delay can be found for example in Dwyer and Aiccroskey (1971), or in Purser and Spearman (1951).

4.3.2   The Effect of the Blade Position Relative to the Nacelle on Aerodynamic Coefficients

Regarding the global consequences of the relative blade position, those shall be compared in terms of AoA, lift- and drag

20 coefficients plotted for the inner rotor half in Fig. 26. The AoA seems generally to increase when flow separation becomes stronger which was already seen for the cases where the nacelle thickness had been increased. Compared to *CaseT1.4*, the axial movement of the blade shows to decrease torque by 0.96% as lift declines and drag slightly rises. The significantly enhanced flow separation in *CaseT1.4dYp05* further deteriorates aerodynamic efficiency being reflected in a decline of torque
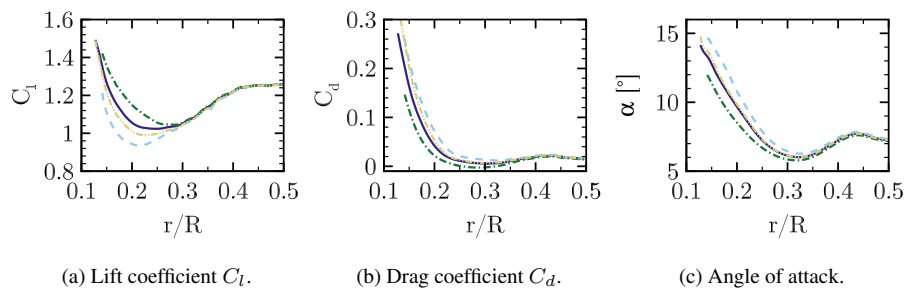
(a) Lift coefficient C_l.   (b) Drag coefficient C_d.   (c) Angle of attack.

Figure 26. Aerodynamic properties along the blade radius for *CaseT1.4* (solid) *CaseT1.4-dXm04* (dashed dot dot), *CaseT1.4-dYm05* (dashed dot) and *CaseT1.4-dYp05* (dashed).

by even 1.98%. *CaseT1.4dYm05* clearly increases lift and decreases drag in the inner portion of the rotor which raises torque by 2.1%. This configuration is already better than *CaseT1.2*, but still around 1.5% worse than *CaseT1.0*. However, as will be shown in the next section, a movement of the blade in direction of rotation based on *CaseT1.0* is able to outperform the aerodynamic behavior of the latter.

4.4 Fillet-Type Modifications in the Junction

The second strategy for a potential reduction of corner separation elaborated in Sec. 4.2.1 was the relief of the boundary layer interaction of blade and nacelle which shall be addressed in this section. The considered configurations modify the geometry of the junction by applying a constant radius of 0.4m all around the airfoil, denoted *CaseT1.0-rounded* and introducing a fairing on the suction side of the blade referred to as *CaseT1.0-fairing*. These modifications are based on *CaseT1.0*. Since the movement of the blade in direction of rotation showed promising results when being based on the largest nacelle, this modification shall be transferred to the smallest nacelle (*CaseT1.0-dYm05*) and be included for comparison in the present discussion. In the rear part the junction reveals a plateau which, from another case not shown here, turned out to be beneficial regarding a restriction of the recirculation area. Since the lateral shift on this nacelle brings along conflicts regarding meshing when moving the blade forward, the periodic segment had to be rotated by $17°$, but due to axisymmetry does not change anything regarding periodicity.

4.4.1 The Effect on Flow Separation and the Corner Vortex System

The streamline plot in Fig. 27 shows that flow separation can be entirely suppressed for *CaseT1.0-dYm05* and *CaseT1.0-fairing*. For the latter quasi two-dimensional flow conditions prevail with only slight streamline deflection close to the trailing edge, whereas the shifted blade again shows the streamline patterns of swept wings. In *CaseT1.0-rounded*, flow separation cannot be noticeably reduced compared to *CaseT1.0* (Fig. 7).

More details on the separation mechanism (and suppression) can be gathered from the vortex system in the corner shown in Fig. 28. Although the footprint of the surface streamlines indicate a similar separation size for *CaseT1.0-rounded* compared to the baseline configuration with sharp junction, recapitulation of Fig. 18 confirms that the separation thickness decreased by
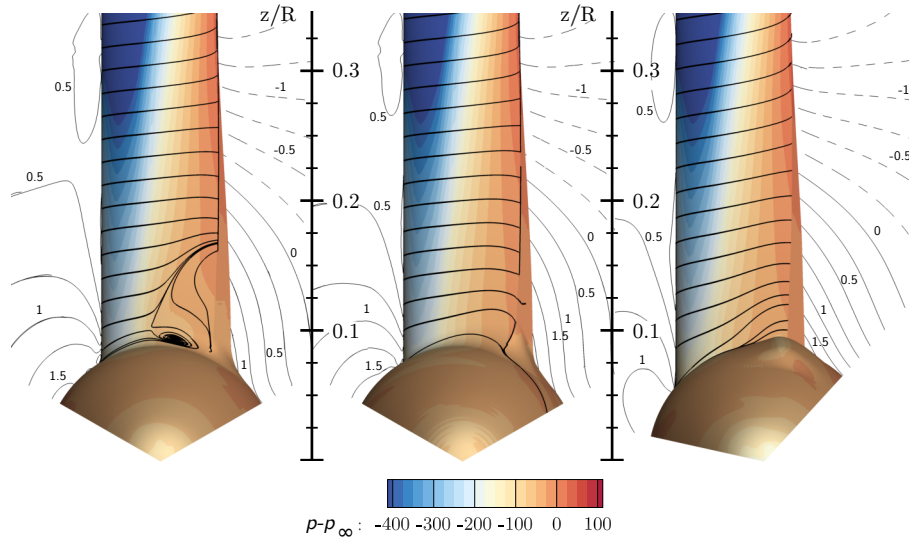
Figure 27. Visualization of three dimensional flow in the root region using streamlines and pressure contours for *CaseT1.0-rounded* (left), *CaseT1.0-fairing* (mid) and *CaseT1.0-dYm05* (right). The contour lines indicate the "deviation velocity" $\tilde{w}$ from to the ideal kinematic value $-\Omega y$ in a slice at $x = 2$m.

introducing the rounding. A side effect of the latter is a weakening of the production of the HSV in the nose region, achieved by a homogenization of the shear layer shown in the foremost slice of the approaching nacelle boundary layer interacting with the blade. Although a streamline counter-rotating to the HSV vortex rotating can be identified in its vicinity, no harmful corner vortex can build up and manifest itself in the junction. Separation is not initiated from a distinct streamline, but forms

5   an isolated vortex generated in the transition from the rounding to the actual blade surface.

These findings were beared in mind in the design of *CaseT1.0-fairing*. It was decided to reduce the fillet nose radius to 0.2m, in order to increase the strength of the HSV again, which is believed to be helpful for reduction of corner separation (Devenport et al., 1992). This is certainly the conservative approach, since the separation should optimally be suppressed in combination with a reduced or even eliminated HSV, as the latter increases the interference drag and is a source of noise (Zess and Thole,

10   2001), (Simpson, 2001), (Devenport et al., 1992). Towards the trailing edge, the local radius was increased on the suction side to eliminate the unfavorable, pressure increasing shape in the transition to the blade of *CaseT1.0-rounded*. As can be seen from the streamlines as well as in the foremost slice, the strength of the HSV could be increased by a factor of three. Its suction side leg remains closer to the blade, as it is not displaced by any recirculation and is deformed ovally when traveling downstream.

In the work of Bordji et al. (2015), the formation of the corner vortex correlated well with a peak in the Reynolds shear

15   stress generated by the chord-wise and span-wise velocity. In order to assess the corner vortex generation for *CaseT1.0* and *CaseT1.0-fairing*, the contours of the $\langle vw \rangle$ shear stress is depicted in Fig. 29 for a slice at $x_c/c = 0.5$. The plot confirms the peak and change in sign of shear stress for *CaseT1.0* similarly as observed in Bordji et al. (2015) and can be therefore seen as clear indicator for the production of the corner vortex. In *CaseT1.0-fairing*, the large rounding radius ensures a smooth mixing of the
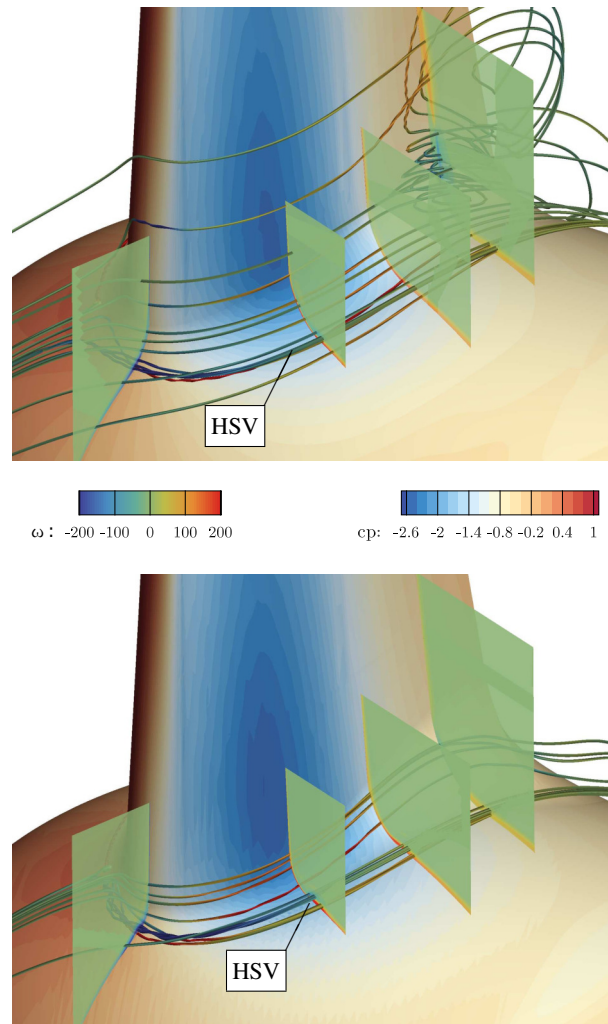
Figure 28. Vortex system in the junction of blade and nacelle for *CaseT1.0-rounded* (upper) and *CaseT1.0-fairing* (lower).

boundary layers resulting in a homogeneous distribution of shear stress which prevents the generation of the CV. Additionally, as it was already suggested by the streamline plot in Fig. 27, the formation of the HSV changes, as well. Its strength is less compared to *CaseT1.0* and it is stretched. The fact that its center is located significantly closer to the blade surface is beneficial regarding its induction on the blade.

5   ### 4.4.2   The Effect of Fillets on Aerodynamic Coefficients

Turning finally to the quantities related to aerodynamic efficiency, the pressure distribution in Fig. 30 clearly shows the improvement obtained by eliminating the corner separation for *CaseT1.0-dYm05* and *CaseT1.0-fairing*. The suction force is
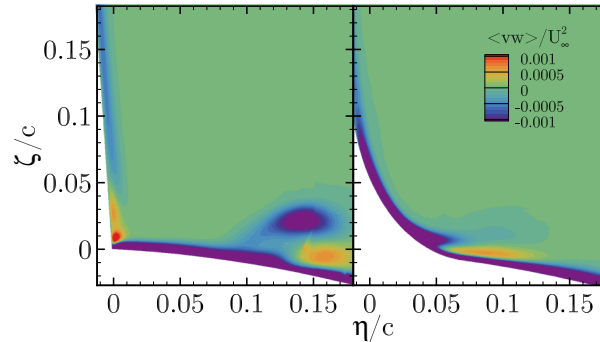
Figure 29. Reynolds shear stress $\langle vw \rangle$ of the chord-wise and span-wise velocity at $x_c/c = 0.5$. *CaseT1.0* (left), *CaseT1.0-fairing* (right).
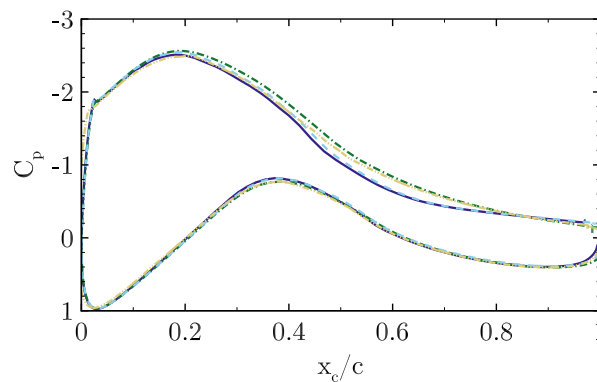

Figure 30. Pressure coefficient at $r/R = 0.136$. *CaseT1.0* (solid), *CaseT1.0-rounded* (dashed), *CaseT1.0-fairing* (dashed-dot), *CaseT1.0-dYm05* (dashed dot dot).

particularly larger between 40-60% chord and the boundary layer is able to stand the adverse pressure gradient which leads to an effectively higher pressure value in the vicinity of the trailing edge.

The attached flow in the corner reduces the AoA (Fig. 31 c)), consistently to the previous observations, being most pronounced for *CaseT1.0-dYm05*. As already indicated by the pressure distribution in Fig. 30, *CaseT1.0-fairing* particularly increases lift and only marginally decrease drag, whereas for *CaseT1.0-dYm05* the improvements are more related to drag. Overall, tangential force increases due to greater lift in *CaseT1.0-fairing* resulting in a boost of torque for the inner 30% of the rotor radius by almost 5.9%. For *CaseT1.0-dYm05* the improvement is still 3.4% compared to the baseline version.

5 Conclusions

Numerical investigations on the flow in the root region of a wind turbine with flatback airfoils have been performed using the CFD code FLOWer.
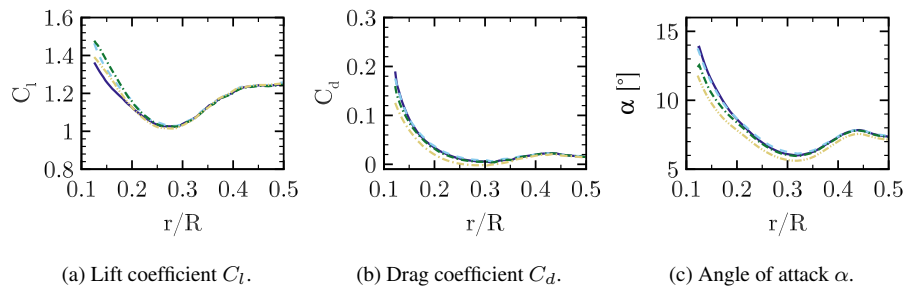
(a) Lift coefficient C_l.   (b) Drag coefficient C_d.   (c) Angle of attack α.

Figure 31. Distribution of aerodynamic coefficients along the blade radius for *CaseT1.0* (solid), *CaseT1.0-rounded* (dashed) *CaseT1.0-fairing* (dashed dot) *CaseT1.0-dYm05* (dashed dot dot).

The flow in the blade root region has been characterized and the influence of the nacelle on the root flow has been elaborated by comparison with an isolated rotor simulation. Regarding the root flow, a corner flow separation has been identified being different to commonly massive flow separation in the root region of conventional turbines with cylindrical root sections. The corner separation is governed by a vortex system evolving in the junction of the blade and the nacelle. Although separation is shallow, the very high solidity of the rotor involves strong three-dimensional effects which are determined by centrifugal and Coriolis forces as well as significant sweep angles. It can be stated that when focusing on blade root aerodynamics for those kind of rotors, a consideration of the nacelle seems to be highly important, as flow topology, aerodynamic coefficients and forces were markedly different when simulating only the isolated rotor.

Following the principal analyses, geometrical properties affecting the blade-nacelle interference had been introduced with the objective to improve the aerodynamic performance of the rotor in the root region. The first parameter investigated was the relative nacelle thickness. By increasing the nacelle thickness, flow separation in the root region drastically increased resulting in power losses for the whole rotor of up to 1.18%. The reasons for the increased flow separation were found from inviscid reference simulations indicating a higher overall adverse pressure gradient for the larger nacelle thickness by means of an unfavorable interaction of the pressure minimums of the blade and the nacelle. An important observation of the viscous simulations was further that the increased nacelle thickness also enhanced the detrimental interaction of the boundary layers in the junction area. From these findings two threads for diminishing the separation had been elaborated, the first was a decoupling of the pressure gradients of the blade and the nacelle and the second aimed for an alleviation of the harmful boundary layer interaction in the junction region.

A shift of the blade forward in axial direction did not improve stall behavior. More effective was the lateral decoupling of the pressure gradients. By moving the blade forward in lateral direction, stall could be effectively reduced, or even eliminated when applied to the smallest nacelle thickness, and with that, aerodynamic efficiency could be increased. The mechanisms for the achieved improvements could be explained by decoupling of the pressure gradients, and kinematic reasons which resulted in higher velocities in the front part of the blade and in the adverse pressure gradient of the junction boundary layer. An effective

sweep angle further assisted the outward transport of separated flow. The shift of the blade in the other direction deteriorated the flow dynamics in the root region compared to the centered base version.

The attachment of fillets in the junction of the blade and the nacelle could be shown to diminish flow separation, as well. Particularly effective was the installation of a fairing, implying a small rounding radius at leading edge and a large radius near the trailing edge of the suction side. With that configuration, separation could be eliminated and torque be increased in the inner 30% of the rotor by 5.9%.

As a final remark it must be stated that this study was meant to demonstrate basic parameters affecting the root flow of a wind turbine with aerodynamically shaped sections down to the hub. Potential for improvement could certainly lie in a detailed parameter optimization of any of the investigated branches. For example it could be aimed to design fillets that prevent separation and effectively alleviate the horse shoe vortex in order to decrease interference drag.

Appendix A: The Effect of the Turbulence Model on Corner Separation

The authors are aware that the prediction of corner flow separation can be rather sensitive to the choice of the turbulence model (Vassberg et al., 2008), (Rumsey et al., 2016). For this reason, a priori simulations of the simplified wing-body junction test case of Gand et al. (2015) have been performed. In principle, this is a wing mounted on a flat plate of a certain length operating at an AoA of $12°$. Three hierarchically different turbulence models have been tested; the one equation SA model (Spalart and Allmaras, 1992), the two-equation k-ω-SST model (Menter, 1994) and the SSG-ω differential Reynolds stress model (Eisfeld, 2004). The results visualizing the corner separation are compared with experimental oil coating in Fig. A1. The SA-model expectedly to literature (Vassberg et al., 2008), (Bordji et al., 2015) greatly over-predicts the amount of separation, whereas the SSG-ω model predicts hardly any separation. In turn, the SST-model provides reasonable results regarding the separation size, with a pattern quite similar to the one obtained by Bordji et al. (2015) using the SA-QCR model (Spalart, 2000). The SST-model further showed meaningful results for vortex properties (HSV and CV) and turbulent kinetic energy (Przewlocki, 2017). As the full RSM is computationally more expensive and further more delicate concerning robustness, it was decided to stick with the SST-model for the considered turbine simulations.

Appendix B: Nomenclature

Symbol	Unit	Description
c	$[m]$	Airfoil chord length
C_d	$[-]$	Drag coefficient
$C_{f,x}$	$[-]$	Chord-wise skin friction coefficient
C_l	$[-]$	Lift coefficient
C_p	$[-]$	Pressure coefficient
d_w	$[m]$	Wall distance

| L | $[m]$ | Length of the nacelle |
p	$[Pa]$	Local static pressure
p_∞	$[Pa]$	Ambient pressure
$q_{\infty,rot}$	$[Pa]$	Kinematic stagnation pressure in the rotating frame
r	$[m]$	Local radius
R	$[m]$	Radius of the blade
u	$[m/s]$	Axial velocity
u_{mag}	$[m/s]$	Velocity magnitude
U_∞	$[m/s]$	Wind speed
$U_{\infty,rot}$	$[m/s]$	Local kinematic inflow velocity in the rotating frame
v	$[m/s]$	Lateral velocity in the rotating frame
v	$[m/s]$	Lateral velocity in the rotating frame
w	$[m/s]$	Vertical velocity in the rotating frame
$\langle vw \rangle$	$[m^2/s^2]$	Reynolds shear stress
$\tilde{w}$	$[m/s]$	Vertical motion relative to the ideal circular path.
x	$[m]$	Axial coordinate
y	$[m]$	Lateral coordinate in the rotating frame
y_p^+	$[-]$	Non-dimensional wall distance wall adjacent cell
z	$[m]$	Vertical coordinate in the rotating frame
x_c	$[m]$	Coordinate in chord-wise direction
α	$[-]$	Angle of attack
Γ	$[m^2/s]$	Bound circulation
η	$[m]$	Blade-normal coordinate normal in the corner frame
ρ	$[kg/m^3]$	Density
Ω	$[1/s]$	Rotational speed
ω	$[1/s]$	Vorticity
ζ	$[m]$	Vertical coordinate in the corner frame
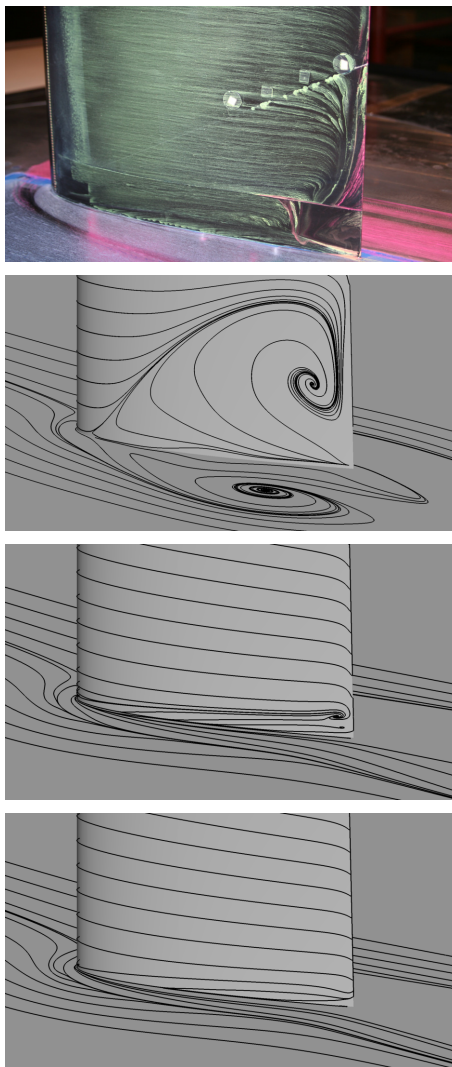
Figure A1. Visualization of corner separation for the simplified wing-body junction experiment of Gand et al. (2015) (upper most). Prediction with SA (upper), SST (mid), and RSM (lower). Figures reproduced from simulations of Przewlocki (2017).

Competing interests. The authors declare that they have no conflict of interest.

References

Akay, B.: The root flow of horizontal axis wind turbine blades: Experimental analysis and numerical validation, 2016.

Bak, C., Zahle, F., Bitsche, R., Kim, T., Yde, A., Henriksen, L. C., Natarajan, A., and Hansen, M. H.: Description of the DTU 10 MW Reference Wind Turbine, http://dtu-10mw-rwt.vindenergi.dtu.dk, 2017.

5 Bangga, G.: Three-Dimensional Flow in the Root Region of Wind Turbine Rotors, Ph.D. thesis, University of Stuttgart, Institute of Aerodynamics and Gas Dynamics, 2018.

Bangga, G., Lutz, T., Jost, E., and Krämer, E.: Erratum:"CFD studies on rotational augmentation at the inboard sections of a 10 MW wind turbine rotor"[J. Renewable Sustainable Energy 9, 023304 (2017)], Journal of Renewable and Sustainable Energy, 10, 019 902, 2018.

Benek, J. A., Steger, J. L., Dougherty, F. C., and Buning, P. G.: in: Chimera. A Grid-Embedding Technique., 1986.

10 Bordji, M., Gand, F., Deck, S., and Brunet, V.: Investigation of a Nonlinear Reynolds-Averaged Navier–Stokes Closure for Corner Flows, AIAA Journal, 2015.

Devenport, W. J., Simpson, R. L., Dewitz, M. B., and Agarwal, N. K.: Effects of a leading-edge fillet on the flow past an appendage-body junction, AIAA journal, 30, 2177–2183, 1992.

Du, Z. and Selig, M.: The effect of rotation on the boundary layer of a wind turbine blade, Renewable Energy, 20, 167–181, 2000.

15 Dwyer, H. and Aiccroskey, W.: Crossflow and unsteady boundary-layer effects on rotating blades, AIAA Journal, 9, 1498–1505, 1971.

Eisfeld, B.: Implementation of Reynolds stress models into the DLR-FLOWer code, 2004.

Gand, F., Monnier, J.-C., Deluc, J.-M., and Choffat, A.: Experimental study of the corner flow separation on a simplified junction, AIAA Journal, 2015.

Guntur, S. and Sørensen, N. N.: A study on rotational augmentation using CFD analysis of flow in the inboard region of the MEXICO rotor
20 blades, Wind Energy, 18, 745–756, 2015.

Herráez, I., Stoevesandt, B., and Peinke, J.: Insight into rotational effects on a wind turbine blade using Navier–Stokes computations, Energies, 7, 6798–6822, 2014.

Herráez, I., Akay, B., van Bussel, G. J., Peinke, J., and Stoevesandt, B.: Detailed analysis of the blade root flow of a horizontal axis wind turbine, Wind Energy Science, 1, 89–100, 2016.

25 Himmelskamp, H.: Profile investigations on a rotating airscrew, MAP, 1947.

Jameson, A.: Time dependent calculations using multigrid, with applications to unsteady flows past airfoils and wings, AIAA paper, 1596, 1991, 1991.

Jameson, A., Schmidt, W., Turkel, E., et al.: Numerical solutions of the Euler equations by finite volume methods using Runge-Kutta time-stepping schemes, AIAA paper, 1259, 1981, 1981.

30 Johansen, J. and Sørensen, N. N.: Aerofoil characteristics from 3D CFD rotor computations, Wind Energy, 7, 283–294, 2004.

Jost, E., Klein, L., Leiprand, H., Lutz, T., and Krämer, E.: Extracting the angle of attack on rotor blades from CFD simulations, Wind Energy. Accepted, 2018.

Knezevici, D., Sjolander, S., Praisner, T., Allen-Bradley, E., and Grover, E.: Measurements of secondary losses in a turbine cascade with the implementation of nonaxisymmetric endwall contouring, Journal of Turbomachinery, 132, 011 013, 2010.

35 Kowarsch, U., Keßler, M., and Krämer, E.: High order CFD-simulation of the rotor-fuselage interaction, 2013.

Kroll, N., Rossow, C.-C., Becker, K., and Thiele, F.: The MEGAFLOW project, Aerospace Science and Technology, 4, 223–237, 2000.

Kühn, T., Altmikus, Daboul, H., Radi, A., Raasch, S., Knigge, C., Böske, L., Schwarz, T., Heister, C., Möller, A., Lutz, T., Weihing, P., Schulz, C., Thiemeier, J., Mockett, C., Fuchs, M., and Thiele, F.: AssiSt-Schlussbericht gemäß NKBF98, Tech. rep.

Leishman, G. J.: Principles of helicopter aerodynamics with CD extra, Cambridge university press, 2006.

Leishman, J.: Modeling sweep effects on dynamic stall, Journal of the American Helicopter Society, 34, 18–29, 1989.

5 Letzgus, J., Dürrwächter, L., Schäferlein, U., Keßler, M., and Krämer, E.: Optimization and HPC-Applications of the Flow Solver FLOWer, in: High Performance Computing in Science and Engineering'17, pp. 305–322, Springer, 2018.

Levy, D. W., Laflin, K. R., Tinoco, E. N., Vassberg, J. C., Mani, M., Rider, B., Rumsey, C. L., Wahls, R. A., Morrison, J. H., Brodersen, O. P., et al.: Summary of data from the fifth computational fluid dynamics drag prediction workshop, Journal of Aircraft, 2014.

Lindenburg, C.: Investigation into rotor blade aerodynamics, ECN Report: ECN-C-03-025, 2003.

10 Loganathan, J. and Gopinath, G.: Advances in Wind Turbine Aerodynamics, 2018.

Menter, F. R.: Two-equation eddy-viscosity turbulence models for engineering applications, AIAA journal, 32, 1598–1605, 1994.

Obert, E.: Aerodynamic design of transport aircraft, IOS press, 2009.

Przewlocki, J.: Numerische Simulation einer vereinfachten Flügel-Rumpf Konfiguration, Master's thesis, University of Stuttgart, Institute of Aerodynamics and Gas Dynamics, 2017.

15 Purser, P. E. and Spearman, M. L.: Wind-tunnel tests at low speed of swept and yawed wings having various plan forms, Tech. rep., NATIONAL AERONAUTICS AND SPACE ADMINISTRATION HAMPTON VA LANGLEY RESEARCH CENTER, 1951.

Rahimi, H., Schepers, G., Shen, W. Z., García, N. R., Schneider, M., Micallef, D., Ferreira, C. S., Jost, E., Klein, L., and Herráez, I.: Evaluation of different methods for determining the angle of attack on wind turbine blades with CFD results under axial inflow conditions, arXiv preprint arXiv:1709.04298, 2017.

20 Rumsey, C. L., Neuhart, D., and Kegerise, M. A.: The NASA juncture flow experiment: Goals, progress, and preliminary testing, in: 54th AIAA Aerospace Sciences Meeting, p. 1557, 2016.

Sayed, M., Lutz, T., Krämer, E., Shayegan, S., Ghantasala, A., Wüchner, R., and Bletzinger, K.-U.: High fidelity CFD-CSD aeroelastic analysis of slender bladed horizontal-axis wind turbine, in: Journal of Physics: Conference Series, vol. 753, p. 042009, IOP Publishing, 2016.

25 Schepers, J. and Snel, H.: Model experiments in controlled conditions, ECN report, 2007.

Schreck, S. and Robinson, M.: Rotational augmentation of horizontal axis wind turbine blade aerodynamic response, Wind Energy, 5, 133–150, 2002.

Schreck, S., Fingersh, L., Siegel, K., Singh, M., and Medina, P.: Rotational augmentation on a 2.3-MW rotor blade with thick flatback airfoil cross sections, in: Proceedings of the 51st AIAA Aerospace Sciences Meeting, AIAA 2013, vol. 915, 2013.

30 Simpson, R. L.: Junction flows, Annual Review of Fluid Mechanics, 33, 415–443, 2001.

Snel, H., Houwink, R., Bosschers, J., Piers, W., Van Bussel, G., and Bruining, A.: Sectional prediction of 3D effects for stalled flow on rotating blades and comparison with measurements, in: Proc. European Community Wind Energy Conference, HS Stevens and Associates, LÃ1, vol. 4, 1993.

Spalart, P. and Allmaras, S.: A one-equation turbulence model for aerodynamic flows, in: 30th aerospace sciences meeting and exhibit, p. 439, 1992.

35 Spalart, P. R.: Strategies for turbulence modelling and simulations, International Journal of Heat and Fluid Flow, 21, 252–263, 2000.

Vassberg, J. C., Tinoco, E. N., Mani, M., Brodersen, O. P., Eisfeld, B., Wahls, R. A., Morrison, J. H., Zickuhr, T., Laflin, K. R., and Mavriplis, D. J.: Abridged summary of the third AIAA computational fluid dynamics drag prediction workshop, Journal of Aircraft, 45, 781–798, 2008.

Weihing, P., Letzgus, J., Bangga, G., Lutz, T., and Krämer, E.: Hybrid RANS/LES capabilities of the flow solver FLOWer-application to flow around wind turbines, in: The 6th Symposium on Hybrid RANS-LES Methods, Strassbourg, 2016.

Weihing, P., Schulz, C., Lutz, T., and Krämer, E.: Comparison of the Actuator Line Model with Fully Resolved Simulations in Complex Environmental Conditions, in: Journal of Physics: Conference Series, vol. 854, p. 012049, IOP Publishing, 2017.

Zess, G. and Thole, K.: Computational design and experimental evaluation of using a leading edge fillet on a gas turbine vane, in: ASME Turbo Expo 2001: Power for Land, Sea, and Air, pp. V003T01A083–V003T01A083, American Society of Mechanical Engineers, 2001.